Available online at www.sciencedirect.com

ScienceDirect

Geochimica et Cosmochimica Acta 323 (2022) 141–163

Geochimica et Cosmochimica Acta

www.elsevier.com/locate/gca

Fluid inclusion $^{40}Ar/^{39}Ar$ geochronology of andalusite from syn-tectonic quartz veins: New perspectives on dating deformation and metamorphism in low-pressure metamorphic belts

Ming Xiao [a,b,c], Yingde Jiang [a,b,*], Guochun Zhao [c,d], Huaning Qiu [e,f], Yue Cai [g,h], Xiujuan Bai [e,f], Chao Yuan [a,b], Wanfeng Zhang [a,b], Lingzhu Kong [a,b,i], Sheng Wang [j]

[a] *State Key Laboratory of Isotope Geochemistry, Guangzhou Institute of Geochemistry, Chinese Academy of Sciences, Guangzhou 510640, China*
[b] *CAS Center for Excellence in Deep Earth Science, Guangzhou 510640, China*
[c] *Department of Earth Sciences, The University of Hong Kong, Pokfulam Road, Hong Kong, China*
[d] *State Key Laboratory of Continental Dynamics, Department of Geology, Northwest University, Northern Taibai Street 229, Xi'an 710069, China*
[e] *Key Laboratory of Tectonics and Petroleum Resources (China University of Geosciences Wuhan), Ministry of Education, Wuhan 430074, China*
[f] *School of Earth Resources, China University of Geosciences, Wuhan 430074, China*
[g] *State Key Laboratory of Palaeobiology and Stratigraphy, Nanjing Institute of Geology and Palaeontology and Center for Excellence in Life and Paleoenvironment, Chinese Academy of Sciences, Nanjing 210008, China*
[h] *Lamont-Doherty Earth Observatory of Columbia University, 61 Rt. 9W, Palisades, NY 10964, USA*
[i] *University of Chinese Academy of Sciences, Beijing 10049, China*
[j] *School of Civil Engineering, Anhui Jianzhu University, Hefei 230601, China*

Received 28 August 2021; accepted in revised form 21 January 2022; Available online 29 January 2022

Abstract

Syn-tectonic quartz veins are widely present in low- to medium-grade metapelitic belts, however, dating these veins is challenging due to the lack of suitable target minerals for most geochronological methods. Andalusite is a common K-poor aluminosilicate mineral in these quartz veins. In this study, we demonstrate the feasibility of dating fluid inclusions in andalusite using the $^{40}Ar/^{39}Ar$ gentle stepwise crushing technique. Three andalusite samples in syn-tectonic quartz veins from the Chinese Altai, Central Asia yielded similar gas release patterns. The first crushing steps generated significant excess ^{40}Ar which likely originated from secondary gas inclusions. These steps gave anomalously old and quickly declining apparent ages. The following crushing steps generated less significant excess ^{40}Ar and yielded concordant and well-defined Early Permian ages of 282–277 Ma. These steps were likely dominated by the degassing of intra-crystal liquid-rich fluid inclusion planes. Two of the crushed powder samples from the stepwise crushing experiments were selected for additional $^{40}Ar/^{39}Ar$ stepwise heating using a furnace and yielded a much younger age of 216 Ma. Laser stepwise heating of muscovite flakes in two of the investigated andalusite samples and one chloridized biotite sample from a different andalusite-bearing quartz vein yielded $^{40}Ar/^{39}Ar$ ages of 243–241 Ma and 214 Ma, respectively. Compared with gases released from the crushing experiments, gases extracted from the heating experiments showed distinct Cl–K–Ca compositional characteristics and younger ages with near atmospheric

---

* Corresponding author at: State Key Laboratory of Isotope Geochemistry, Guangzhou Institute of Geochemistry, Chinese Academy of Sciences, Guangzhou 510640, China.
E-mail address: jiangyd@gig.ac.cn (Y.D. Jiang).

https://doi.org/10.1016/j.gca.2022.01.025

initial ^{40}Ar/^{36}Ar value. These observations suggest that 1) contrary to common wisdom, excess ^{40}Ar in K-poor nesosilicates are preferably preserved in fluid inclusions rather than mineral lattices, and 2) K (Ar) contamination from K-bearing solid phases is negligible during gentle stepwise crushing. As such, the 282–277 Ma fluid inclusion ^{40}Ar/^{39}Ar ages could be considered as the timing of andalusite growth in the quartz veins. The younger muscovite ^{40}Ar/^{39}Ar ages likely record more recent cooling events. The youngest ^{40}Ar/^{39}Ar ages of the crushed andalusite powder and the biotite sample could reflect the timing of sericitization and chloritization of the samples, which is evidenced by petrologic observations and x-ray K mapping results. Furthermore, andalusite ^{40}Ar/^{39}Ar ages agree with the monazite/zircon U–Pb ages (280–273 Ma) of syn-tectonic leucogranite and pegmatite dykes and metamorphic ages (299–262 Ma) for the low-pressure metamorphic rocks of the region. These results suggest that fluid inclusion ^{40}Ar/^{39}Ar geochronology of andalusite can be used to constrain the timing of deformation and associated metamorphism in low-pressure metapelitic terranes, which can also provide more complete pictures of the tectono-thermal evolution in combination with traditional ^{40}Ar/^{39}Ar stepwise heating geochronology.

Keywords: Andalusite; Syn-tectonic quartz veins; ^{40}Ar/^{39}Ar stepwise crushing; Tectono-thermal evolution; Metapelitic terranes

1. INTRODUCTION

Fluids play an important role in the physical, chemical, and mechanical evolution of the continental crust as their presence and circulation facilitate mass and heat transfer, fluid-rock interaction, hydrocarbon migration, mineralization, and partial melting at depth (e.g., Lacombe and Rolland, 2016). Fluid activity is also important during orogeneses, which is best exemplified by the occurrence of abundant quartz, quartzo-feldspathic, and pegmatite veins and/or dykes at different scales varying from micrometers to several kilometers (Bons, 2001; Bakker and Schilli, 2016; Lv et al., 2018).

Geofluids in orogenic belts can derive from a variety of sources, including fluids in the pore spaces of original sediments, shallow meteoric water, mantle and magma degassing, and devolatilization and/or decarbonation reactions of metamorphic rocks (Chapman, 1950; Connolly, 1997; Kennedy and Van Soest, 2007; Menzies et al., 2014; Mancktelow et al., 2015). Veins forming at similar pressure–temperature conditions as the host rocks can generally reach chemical and isotopic equilibrium with the host rocks and thus record the age of local metamorphism (Whitney and Dilek, 2000; Sepahi et al., 2004). Alternatively, some fluids may travel great distances and evolve over several distinct steps, e.g., through successive metamorphic dehydration reactions of regional metamorphic rocks during burial or contact metamorphism, and form deformation-controlled veins that are structurally related to the deformation (Bucholz and Ague, 2010). The ages of these veins would correspond to the timing of deformation or metamorphism, which carry crucial information of regional tectono-thermal processes (Oliver, 1996; Fitz-Diaz et al., 2019).

In high-grade metamorphic terranes where partial melting occurs, anatectic granite, pegmatite and/or leucosome dykes are very common (e.g., Nabelek and Peter, 1997; Wang et al., 2017). These rocks can be dated using available modern geochronological methods, such as zircon and monazite U–Pb dating (e.g., Broussolle et al., 2018; Xu et al., 2021). In contrast, fluid flow commonly forms quartz veins in vast low- to middle-grade terranes where partial melting is limited or absent (Bons, 2001; Sepahi et al., 2004). These are much more difficult to date owing to the lack of suitable target minerals for existing dating methods.

Even though zircon and monazite are occasionally found in some quartz veins, linking their ages with the deformation/metamorphism processes is difficult because their origins are often obscure (Zheng et al., 2007b; Fitz-Diaz et al., 2019). Some K-bearing minerals such as micas have also been reported from metamorphic quartz veins (Daele et al., 2020), and they are, in theory, the best target for ^{40}Ar/^{39}Ar geochronology. However, given their low to middle closure temperatures (T_C) for Ar, e.g., *ca.* 405–425 °C for muscovite (Harrison et al., 2009) and *ca.* 310–330 °C for biotite (Harrison et al., 1985; Grove and Harrison, 1996), ^{40}Ar/^{39}Ar ages of these minerals would represent the age of cooling evolution rather than formation. Additionally, recrystallization or fluid-assisted deformation could lead to partial or complete rest of the K/Ar geological clock of micas (Di Vincenzo et al., 2001, 2004; Villa et al., 2014; Villa, 2016; Bosse and Villa, 2019). Notably, a recent study suggested that tourmaline has a higher Ar T_C around 534–628 °C (Thern et al., 2020) and thus could be a candidate for dating vein formation using stepwise heating ^{40}Ar/^{39}Ar geochronology.

Metamorphic quartz veins in metapelitic terranes commonly contain aluminosilicate minerals such as kyanite, sillimanite, and andalusite megacrystals, which could have shared similar metamorphic conditions with the host rocks (Cesare, 1994; Whitney and Dilek, 2000; Sepahi et al., 2004). While aluminosilicate polymorphs share identical chemical compositions, they have different crystal structures. Kyanite generally occurs as long and slender bladed crystals or flat tabular crystals, whereas sillimanite usually occurs as fibrous or radiating crystals. Andalusite most often occurs as prismatic or blocky crystals which permit better preservation of paleo-fluids in fluid inclusions (Masoudi et al., 2009; Bakker and Schilli, 2016). Metamorphic fluids commonly contain sodium (Na), minor calcium (Ca), and a certain amount of potassium (K) from tens to tens of thousands ppm as revealed by previous LA-ICP-MS analysis on fluid inclusions in quartz veins hosted by different metamorphic rocks (Rauchenstein-Martinek et al., 2016). Paleo-fluids preserved in andalusite fluid inclusions could therefore serve as suitable targets for fluid inclusion $^{40}Ar/^{39}Ar$ geochronology.

Since the 1980s, $^{40}Ar/^{39}Ar$ stepwise crushing has been successfully applied to many minerals such as quartz, K-feldspar, sphalerite, cassiterite, and wolframite associated with hydrothermal quartz veins or sedimentary rocks (Qiu and Dai, 1989; Turner and Wang, 1992; Harrison et al., 1993; Qiu and Jiang, 2007; Bai et al., 2013). This technique was also successfully applied on fluid inclusion-bearing metamorphic minerals such as garnet and amphibole from ultra-high metamorphic rocks or associated veins to constrain the timing of metamorphic evolution (Qiu and Wijbrans, 2006; Qiu et al., 2010; Hu et al., 2015, 2018). Dating paleo-fluids trapped in fluid inclusions in andalusite from syn-tectonic veins is potentially a new way to constrain the timing of deformation and metamorphism in low- to middle-grade metamorphic terranes, in particular, in low-pressure metamorphic terranes.

In this study, we tested $^{40}Ar/^{39}Ar$ stepwise crushing geochronology on andalusite from a well-studied metapelitic domain of the Chinese Altai, Central Asia for the first time. Based on detailed petro-structural observations and compositional analysis, as well as U–Pb dating of monazites from adjacent syn-tectonic leucogranite dykes, we demonstrate that andalusite can be dated using this technique to constrain the age of the syn-tectonic quartz veins and the timing of the associated deformation and metamorphism in low- to middle-grade metapelitic terranes. This method greatly expands our ability to study regional metamorphic and deformation evolution in general.

2. OVERVIEW OF THE FLUID INCLUSION ^{40}AR/^{39}AR GEOCHRONOLOGY

When a given mineral grew and evolved with the presence of fluids, its tiny crystal cavities or micro-fissures could capture the fluids to form fluid inclusions. Fluid inclusions trapped during the initial growth of the host mineral are primary (PFIs) and those captured during nearly simultaneous processes along intra-crystal micro-cracks or later processes along inter-crystal micro-cracks are pseudosecondary (PSFIs) or secondary fluid inclusions (SFIs), respectively (Roedder, 1984; Goldstein et al., 2003). PSFIs are usually not distinguishable from PFIs as they trap similar primary fluids during mineral growth.

Fluid inclusions are unique recorders of the physicochemical nature of the fluids as well as the timing when they get trapped (Shepherd and Darbyshire, 1981; Crawford and Hollister, 1986; Brown and Lamb, 1989; Boullier, 1999; Bodnar et al., 2014). The establishment and development of the fluid inclusion $^{40}Ar/^{39}Ar$ stepwise crushing technique opened a new chapter for geofluid geochronology (Kelley et al., 1986; Qiu and Dai, 1989). Tremendous achievements were made when the technique was widely applied to constraining the time-scales of hydrocarbon migration and accumulation using igneous quartz (Yun et al., 2010; Qiu et al., 2011), metamorphism evolution using garnet (Qiu and Wijbrans, 2006) and amphibole (Qiu et al., 2010; Hu et al., 2015, 2018), as well as metal mineralization events using quartz, sphalerite, wolframite, and cassiterite (Qiu and Dai, 1989; Qiu and Jiang, 2007; Bai et al., 2013; Xiao et al., 2019). The improved stepwise crushing technique with gentle crushing strength can progressively extract most of the SFIs that are larger, irregular, and associated with micro-cracks and smaller PFIs that form from relatively stable fluid flow during the first and last crushing steps, respectively (Xiao et al., 2019, 2022). When combined with $^{40}Ar/^{39}Ar$ geochronology, the ages of SFIs and PFIs can be successively dated using this technique (Qiu and Jiang, 2007; Jiang et al., 2012; Xiao et al., 2019).

In addition to fluid inclusions, solid phases such as K-bearing mineral impurities and lattice-hosted positions could be important Ar reservoirs (Villa, 2001; Kendrick, 2007). It has been noted by several studies that a prolonged crushing process with heavy crushing strength and/or elevated numbers of crushing, e.g., around or more than ten thousand strokes, could extract gases from lattice-hosted positions and solid impurities (e.g., Scarsi, 2000; Kendrick and Phillips, 2009). On the other hand, many studies have proposed that the gentle stepwise crushing technique can avoid extracting gases from these solid phases by utilizing the free fall of a light pestle from a height of 3–4 cm to crush minerals (Qiu and Jiang, 2007; Qiu et al., 2011). In the latter case, the crushing strength can be more than an order of magnitude lower than the traditional air-actuated *in vacuo* crushing devices based on the design of Matsumoto et al. (2001). Such a low crushing strength permits the crusher to mainly extract gases from mineral-hosted fluid inclusions with very limited contaminations from K-bearing solid phases (Jiang et al., 2012; Bai et al., 2013). When the crushing process is coupled with quadrupole mass spectrometer analyses, we found that gases released by gentle stepwise crushing showed elevated release of large gas molecules such as C_2H_6, C_3H_8, N_2, formamide, and/or CH_4 after 9000 drops of crushing (drop represents the time that the pestle falls), which suggests that these gases are mainly derived from fluid inclusions (Xiao et al., 2019, 2021). Due to the very low partition coefficients between mineral and hydrous fluids, fluid inclusions should dominate the Ar budget in K-poor minerals (Kelley, 2002; Baxter, 2003). Therefore, the trace amounts of K hosted in mineral lattices should not influence the validity of the ages. Alternatively, stepwise heating of the crushed residues can effectively release K-derived argon from solid phases (e.g., Qiu and Jiang, 2007; Hu et al., 2015). It has also been shown that the extracted gases from crushing and subsequent heating processes showed distinct compositions and, sometimes, different $^{40}Ar/^{39}Ar$ ages (e.g., Qiu and Jiang, 2007; Qiu et al., 2010; Hu et al., 2015). This is consistent with the notion that contributions of argon gases trapped in mineral lattices and impurities during gentle stepwise crushing would be negligible, if not impossible.

3. GEOLOGICAL SETTING

3.1. Regional geological framework

The Altai orogenic belt, evolved from the Altai accretionary wedge, is located in the hinterland of the Central Asian Orogenic Belt (CAOB, also known as Altaids,

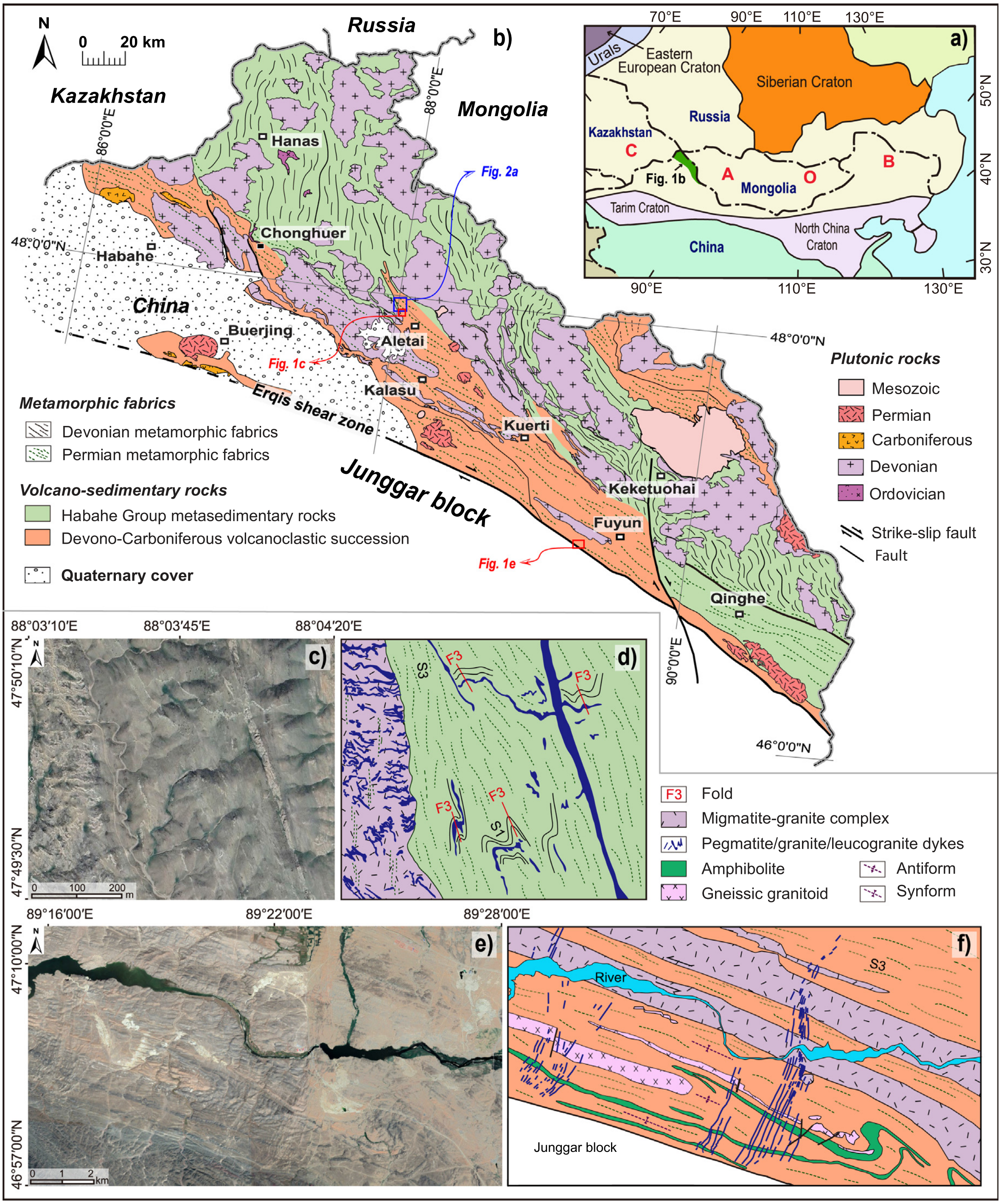

Fig. 1. (a) Simplified map showing the location of the Chinese Altai in the Central Asian Orogenic Belt (CAOB). (b) Geological map of the Chinese Altai (modified after Broussolle et al. (2019)). Satellite and geological maps showing occurrences of syn-tectonic veins/dykes in the NW of the Aletai city (c–d) and the SW of the Fuyun City (e–f). The geological maps d and f are modified after Jiang et al. (2019) and Li et al. (2017), respectively.

Fig. 1a) which represents the largest Phanerozoic accretionary orogenic belt on Earth (Şengör et al., 1993; Şengör and Natal'In, 1996; Xiao et al., 2004; Kröner et al., 2007; Windley et al., 2007; Xiao et al., 2009, 2015). The CAOB has been recently considered to form via amalgamation of three collage systems at its termination stage: the Kazakhstan Collage in the west, the Mongolian Collage in the east, and the Tarim-North China Collage in the south, from Late Carboniferous to Early Mesozoic (Xiao et al., 2015). The collision of the newly formed and accreted crustal components and the development of large-scale transpressional zones associated with near N-S shortening mark the final amalgamation of the Mongolian collage (Laurent-Charvet et al., 2003; Lehmann et al., 2010; Xu et al., 2021). The Chinese Altai orogenic belt, lying along the southwest margin of the early Paleozoic active margin of the Mongolian continental blocks, is separated from the Devono-Carboniferous oceanic arc domain of East Junggar in the south by the NW-trending Erqis fault zone (Fig. 1b, Xiao et al., 2009; Jiang et al., 2017). The Erqis fault zone represents a regional-scale transpressional zone that records shortening-convergence and/or collision between the Chinese Altai and the southern East Junggar which evolved during a period mainly of *ca.* 295–250 Ma (Qu and Zhang, 1994; Laurent-Charvet et al., 2003; Briggs et al., 2007; Li et al., 2015, 2017; Xu et al., 2021).

The Chinese Altai region preserved excellent records of Devonian and Permian tectono-thermal cycles (Qu and Zhang, 1994; Broussolle et al., 2018; Jiang et al., 2019). The Devonian tectono-thermal cycle occurs throughout the Chinese Altai (Fig. 1b) and is characterized by a multiphase metamorphic-tectonic history (Jiang et al., 2015; Broussolle et al., 2019; Jiang et al., 2019). The earliest known tectono-thermal event (termed D1) is characterized by an early burial and thickening phase and a subsequent extension at *ca.* 410–400 Ma. During the extension, earlier Barrovian-type middle temperature/middle pressure (MT/MP) fabrics were overprinted by high temperature/low pressure (HT/LP) metamorphism and the crust was stretched and thinned (Broussolle et al., 2019; Jiang et al., 2019). The extension was also accompanied by regional-scale crustal anatexis, widespread intrusion of circum-Pacific S-type granitoids, and extensive eruption of volcanics with bimodal geochemical signatures (Wang et al., 2006; Yuan et al., 2007; Cai et al., 2011; Jiang et al., 2016; Cui et al., 2020). The stretched crust was soon after affected by a 400–380 Ma deformation phase of horizontal shortening designated D2 forming regional-scale upright folding and juxtaposition of diverse rocks from different crustal levels (Zhang et al., 2015; Jiang et al., 2019). The Devonian tectono-metamorphic cycle marked by the above-cited successive burial-thickening (shortening), extension, and shortening evolution was considered as a coaxial suprasubduction sequence of tectonic switching of an advancing and retreating subduction system (Jiang et al., 2019).

The Permian tectono-thermal cycle is less extensive than the Devonian one. The Permian structures (designated D3) are mainly restricted to the southern Chinese Altai (Fig. 1b) and show a general decrease in deformation intensity from south to north. In the southernmost part, it caused SSW-ward thrust systems as well as tight upright to overturned folds associated with the development of penetrative WNW-ESE-striking schistosity (designated S3), almost perpendicular to the Devonian structures (Qu and Zhang, 1994; Briggs et al., 2007). Further north, the pre-existing Devonian structures are rotated and in part transposed into a WNW-ESE-directed orientation (Zhang et al., 2012; Broussolle et al., 2018; Jiang et al., 2019). D3 was dated between 290 and 260 Ma (Briggs et al., 2007; Li et al., 2017). A coeval metamorphic event characterized by the occurrence of low-pressure/(ultra) high-temperature metamorphic assemblage has been reported from many migmatite and granulites along the southern Chinese Altai (Wang et al., 2009; Li et al., 2014; Tong et al., 2014; Liu et al., 2020). The deformation and metamorphism are commonly interpreted as an overall response to nearly SSW-NNE-directed collision between the Chinese Altai and the southerly Junggar arc domain (Li et al., 2016, 2017; Jiang et al., 2019).

Numerous quartz veins associated with leucogranite and pegmatite dykes, varying from a few decimetres to several kilometers long, were emplaced within the Permian deformation zone along the southern flank of the Chinese Altai (Figs. 1–4). Unlike the Devonian dykes/veins (if any) that could be affected by extensive Permian deformation, these Permian ones still preserved their original structures and as such, they could be used to decode the Permian deformation. Recent structural analysis on the Permian deformation domain along the southern Chinese Altai revealed progressive northward propagating tensional fractures associated with the northward development of folding in response to the Altai-Junggar collision (Jiang et al., 2019). When the dykes/veins were emplaced at the tensional fractures at the collision front where D3 folding was already locked, they were undeformed and orthogonally crosscut the Permian folds (Fig. 1e–f). In contrast, when dykes/veins were emplaced at the interior of the Chinese Altai further to the north where D3 folding was actively growing, they were variably folded, i.e., gently folded in more competent granites and tightly folded in less competent micaschists (Fig. 1c–d and Fig. 3a–c). In the latter case, the dykes/veins were rotated to varying degrees, some even nearly parallel to the axial plane (see sketches in Fig. 3f). Restoration of the geometries of the dykes/veins in the interior zone shows that their original orientations were also orthogonal to S3 foliation (Jiang et al., 2019). Based on these lines of evidence, the dykes/veins that cropped out in the collisional front and in the Chinese Altai interiors have consistent original NE-SW-directed orientations, which is parallel to the principal compressive stress of the D3 shortening. These pieces of information indicate that these veins/dykes were emplaced during the D3 event. This conclusion is further supported by zircon and monazite U–Pb age data of these leucogranites and pegmatites, which yielded dominantly 280–270 Ma formation ages, overlapping in timing with D3 (Briggs et al., 2009; Zhang et al., 2012; Li et al., 2017; Broussolle et al., 2018; Jiang et al., 2019). These Permian dykes are geochemically comparable with the metasediments in the southern Chinese Altai where partial melting of the metasediments was dated as roughly contemporaneous with the dyke emplacements, leading many to suggest that the dykes were derived from local metasedimentary rocks (Hu et al., 2021; Lv et al., 2021).

Except for the prominent Devonian and Permian tectono-metamorphic events, the Chinese Altai also recorded less significant Triassic magmatism (Fig. 1). This is exemplified by the occurrence of small and isolated granitoid bodies such as the Shangkelan pluton (209–203 Ma), the Alaer pluton (216–210 Ma), and the Xibuodu pluton (*ca.* 213 Ma) as well as the world-famous Keketuohai pegmatites (220–209 Ma) in the southern Chinese Altai (Wang et al., 2007; Liu et al., 2014; Wang et al., 2014a; Lin et al., 2019). These granitoids were collectively regarded as

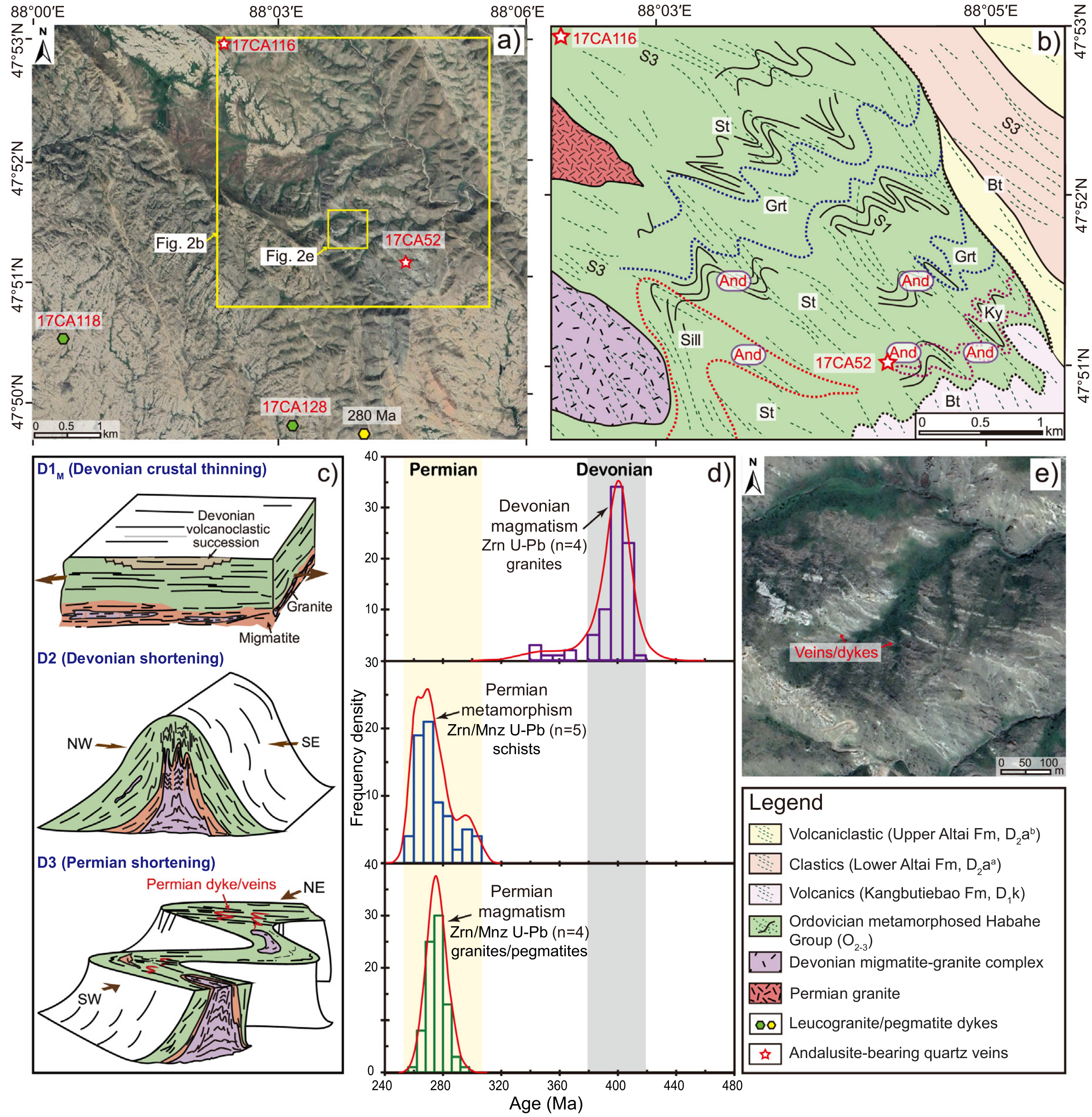

Fig. 2. (a) Satellite image showing the extent of the study area. Locations of the mapping areas and samples are shown. (b) Map view showing the occurrences of index metamorphic minerals and associated metamorphic isograds (indicated by thick dashed lines). The presence of andalusite in local domains is highlighted. Planar structures including S1 transposed by S3 fabric are also indicated (modified after Jiang et al., 2019). (c) Simplified sketches showing Devonian and Permian tectono-thermal evolution in the study region (not to scale, modified after Jiang et al. (2021b)). (d) Histograms showing published age data of regional magmatic-metamorphic activities. Data are from Wang et al. (Wang et al., 2006; Wang et al., 2014b; Jiang et al., 2019; Jiang et al., 2021b). (e) Satellite image showing the distribution of meter-scale pegmatite dykes and/or quartz veins. Bt-biotite, Grt-garnet, St-staurolite, Ky-kyanite, Sill-sillimanite, And-andalusite, Zrn-zircon, and Mnz-monazite.

post-collisional intrusions (Wang et al., 2014a; Lin et al., 2019; Liu and Han, 2019).

3.2. Geology of the sampling area

This study focuses on a specific region located northwest of the Aletai city (Fig. 2a). The key lithological and metamorphic sequences are divided into three major packages (Li et al., 2016; Jiang et al., 2019): 1) a high-grade migmatite-granite complex representing the deep rocks in the west, 2) a metamorphosed but not molten Habahe Group metasedimentary sequence in the center, and 3) a weakly- to un-metamorphic volcanoclastic Devonian succession in the east (Fig. 2b).

The migmatite-granite complex consists of predominant granites and subordinate migmatitic paragneisses. Zircon U–Pb studies of the granites gave ages ranging from 401 to 368 Ma, with a dominant peak at *ca.* 400 Ma (Fig. 2d, Wang et al., 2006; Cai et al., 2011; Jiang et al., 2019). The metamorphosed Ordovician Habahe Group is originally greywacke-dominated turbidites associated with subordinate volcanogenic sediments (Long et al., 2008;

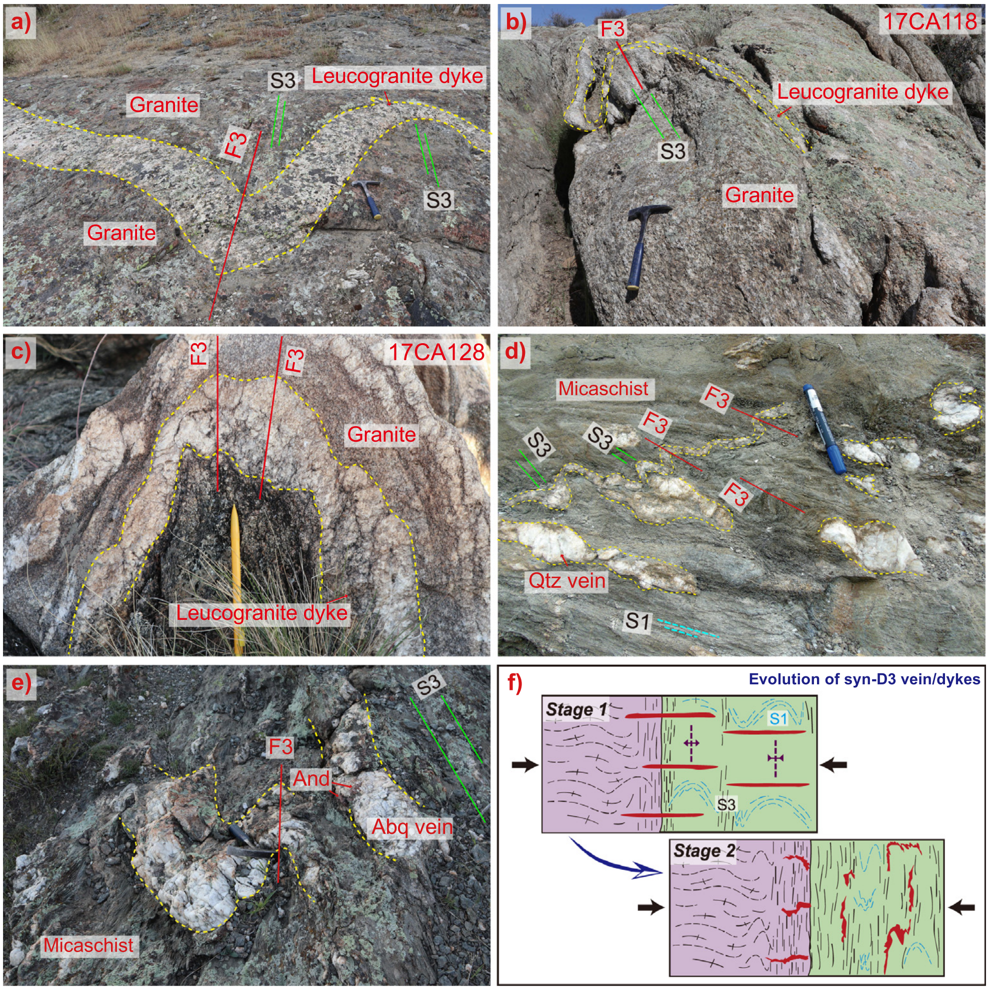

Fig. 3. Outcrop photographs and structural characteristics of leucogranite dykes intruding the migmatite-granite complex (a–c) and of quartz veins occurring in the micaschists (d–e) in the study area. Abq vein refers to andalusite-bearing quartz vein. (f) Sketches showing the evolution of syn-D3 dykes/veins during Permian shortening.

Huang et al., 2020) and now consists mainly of amphibolite-facies coarse-grained micaschists interlayered with quartzo-feldspathic rocks (Jiang et al., 2019). It is covered by Devonian sedimentary sequences that mainly consist of the volcano-clastic Kangbutiebao Formation in the lower part and siliciclastic sediments, fossiliferous limestones to volcanoclastic rocks of the Altai Formation in the upper part (Windley et al., 2002). Zircons from felsic volcanic rocks of the Altai Formation yielded an eruption age of *ca.* 396 Ma (Jiang et al., 2019), similar to the major age population of the schlieren-rich granites from the west.

The study area records multiple phases of tectono-metamorphic evolution as revealed by the studies of Li et al. (2016) and Jiang et al. (2019, 2021b). Their main findings are summarized below (also see tectonic sketches in Fig. 2c). The oldest tectono-metamorphic event is well preserved in the metamorphosed Habahe Group, as exemplified by a ubiquitous Barrovian-type metamorphic fabric known as $S1_B$, in response to regional burial and crustal thickening phase of D1 deformation (Fig. 2b). This fabric was affected by a subsequent extensional phase (*ca.* 400 Ma) of the same deformation forming a $S1_B$-parallel migmatite-magmatic foliation, namely $S1_M$, in the migmatite-granite complex (Fig. 2b). Both $S1_B$ and $S1_M$ foliations were affected by crustal-scale NE-SW striking upright F2 folding, which was suggested as the consequence of regional NW-SE-orientated D2 shortening that occurred soon after the extensional phase of deformation (Fig. 2c). As a result, the preexisting fabrics were rotated into moderately dipping sub-vertical positions, and metamorphic isograds and zones from different crustal levels were juxtaposed at the shallow crustal levels (Fig. 2b). Less commonly, the S1 was transposed and formed steep S2 foliation in places.

The study area was further affected by a prominent D3 deformation characterized by an important NE-SW shortening (Fig. 2c). This event formed a large number of NW-SE-trending vertical D3 high-strain zones where S1 foliation was transposed into penetrative S3 foliation alternating with low-strain domains where F2 folds were refolded (Fig. 1c–d). The latter is characterized by tight-to-open F3 folds in scales varying from millimeters

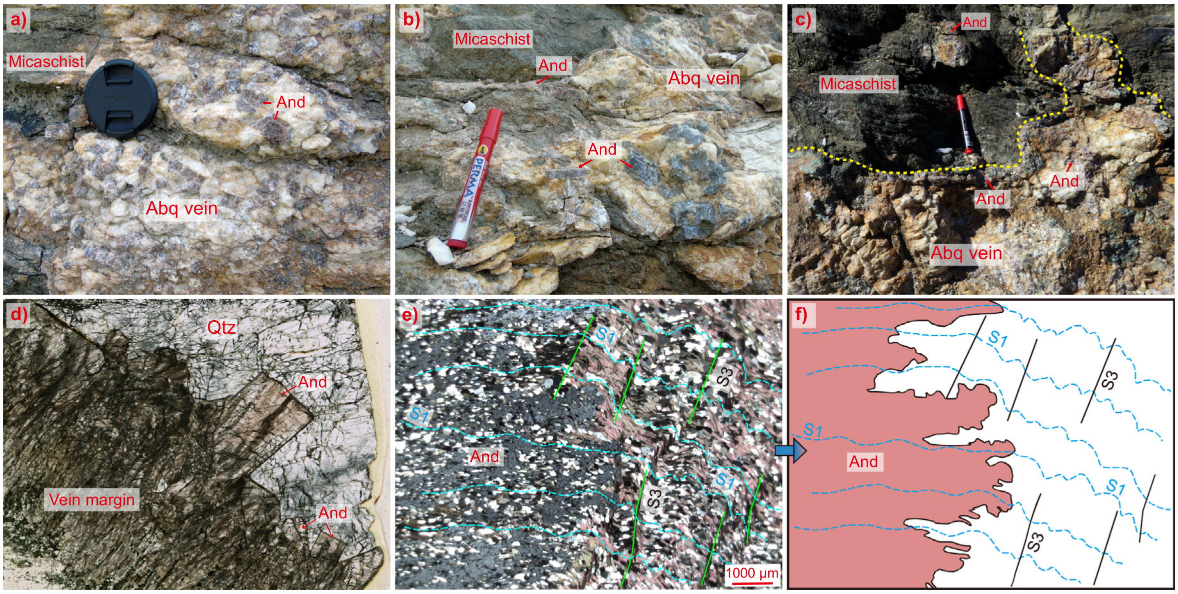

Fig. 4. (a–d) Photographs of andalusite-bearing quartz veins hosted in micaschists. (e–f) Andalusite porphyroblast overgrows the F3 crenulations. See text for details.

to dozens of meters. The timing of D3 shortening was constrained to 280–273 Ma by zircon and monazite U–Pb ages of syn-D3 granite intrusions and pegmatite dykes (Fig. 2d, Jiang et al., 2019). More recent findings suggested that syn-D3 growth of andalusite- and less commonly cordierite-bearing assemblages forming a few tens to several hundred meters of discontinuous HT/LP domains in the vicinity of pegmatite dykes of Permian ages and quartz veins of unknown ages (Jiang et al., 2021b). The inferred pressure–temperature evolution of the HT/LP domains suggests significant heating processes with peak metamorphic conditions that largely fall in a range of 3.0–5.0 kbar/550–600 °C, which correspond to an apparent thermal gradient of 40 °C/km or more (Wei et al., 2007; Jiang et al., 2021b). *In-situ* U–Pb dating of monazite inclusions in andalusite and cordierite yielded ages of 279–268 Ma, which is interpreted as the growth age of these minerals (Fig. 2d, Jiang et al., 2021b).

4. SYN-TECTONIC D3 ANDALUSITE-BEARING QUARTZ VEINS

4.1. Structural characteristics of syn-tectonic quartz veins

Abundant quartz veins, ranging from centimeters to dozens of meters wide, occur mainly in the metamorphosed Habahe Group rocks in the study region (Fig. 2e). They always crosscut the steep $S1_B$ foliation of the host rocks and are commonly folded by D3 (e.g., Fig. 3d–e). In places, the quartz veins are re-orientated, some even parallel to axial planes of F3 folds. They are strongly flattened and boudinaged within the transposed S3 foliation (Fig. 3d–e). In the low strain domains, characteristic cleavage refraction in the folded quartz veins can be observed (e.g., Fig. 3e). When unfolding the quartz veins, they are almost perpendicular to the regional S3 foliation. These features are consistent with quartz veins being initially emplaced orthogonal to the XY plane of the D3 strain ellipsoid (i.e., parallel to principal compressive stress, Fig. 3f). The deformation continued after the vein emplacement and solidification (Fig. 3f), thereby indicating syn-D3 emplacement of the veins.

In addition, thickening of the quartz veins in F3 fold hinge zones and thinning along the limbs are common (Fig. 3d–e). This may reflect deformation-induced dilatancy and permeability enhancement that could have driven the fluids transferring from high-pressure (fold limbs) to low-pressure zone (fold hinges) (Chapman, 1950; Yardley and Bottrell, 1992; Oliver, 1996), which further indicates syn-kinematical emplacement of the quartz veins with D3 deformation.

These quartz veins contain a large number of andalusite crystals (Fig. 4a–d). These andalusite minerals exhibit different features according to their spatial distributions. Andalusites occurring in the center part of the quartz vein are idiomorphic prisms (up to 10 cm) without preferred orientations (Fig. 4a–c), whereas those located at the marginal zone of the vein or some veinlets generally occur in the form of columnar aggregates (<2 cm) or blocky (<5 cm) crystals perpendicular to the vein walls (Fig. 4b–d). Notably, spatially discontinuous andalusite-bearing domains, varying in sizes from a few dozen meters to several hundred meters, form in the micaschists surrounding regions of intense quartz veining (Fig. 2b). This suggests an important role of hydrothermal activity on the crystallization of low-pressure metamorphic assemblages in the metamorphic Habahe Group rocks.

In the host micaschists, andalusite porphyroblasts overgrew F3 crenulations (Fig. 4e). In this case, intensification of the F3 crenulations at the margins of some andalusite grains can also be observed (e.g., Fig. 4e–f).

These features suggest that andalusite growth occurred during variable stages of D3 deformation. It started after the beginning of the F3 crenulation and ended while the D3 deformation was ongoing. Additionally, development of S3 strain shadows around the andalusite porphyroblasts was also reported from the host micaschists (Jiang et al., 2021b), advocating syn-D3 growth of the andalusites. Based on these observations, the growth of andalusites in quartz veins was synchronous with metamorphic reactions taking place in the host rock at the time of vein formation.

4.2. Petrographic characteristics

Three andalusite samples from syn-tectonic quartz veins were collected for petrographic observations. Samples 17CA52-1 and 17CA52-2 are collected from different quartz veins in the same outcrop. Sample 17CA52-1 consists of isolated prismatic crystals (up to 7 cm in length) in the center of a meter-scale large quartz vein. By contrast, sample 17CA52-2 consists of columnar crystals (up to 2 cm in length) in the margin of a decimeter-scale quartz vein lens. Sample 17CA116 composed of blocky crystals (3 cm in length) was collected near the margin of a decimeter-scale quartz vein from another outcrop. Locations of these samples are indicated in Fig. 2. Despite dissimilar macrostructures, these andalusite crystals are similarly euhedral and fractured (Fig. 5a–e). They are almost pure aluminosilicates ($SiO_2 = 35.80–37.25$ wt.% and $Al_2O_3 = 61.44–63.24$ wt.%) containing minor FeO (0.71–1.20 wt.%) and very low CaO (0–0.02 wt.%) and K_2O (0–0.01 wt.%) contents (Table S1).

Considerable amounts of euhedral muscovite, up to a few centimeters in size, are found as intergrowths in samples 17CA52-1 and 17CA52-2 (Fig. 5a–c). Sharp and clean grain boundaries between muscovite and andalusite suggest contemporaneous growth (Fig. 5a–c). Andalusite crystals of sample 17CA116 do not contain large mica inclusions (Fig. 5d–e). Fine-grained muscovite aggregates (sericite) are widely present in all the samples (Fig. 5b–e), which suggests sericitization during secondary hydrothermal events. Combined petrologic observations and EPMA (electron probe microanalysis) results revealed two types of sericites, i.e., high- and low-K, present in andalusite samples 17CA52-1 and 17CA52-2 (mostly occur along alteration fractures and margins of both muscovite and andalusite crystals, Fig. 5b–c) and only low-K sericites present in andalusite sample 17CA116 (occur along interior fractures and/or crystal margins, Fig. 5e). The low-K sericites have much lower K_2O contents (0.56–3.62 wt.%) than those of the high-K sericites ($K_2O = 6.06–8.48$ wt.%) and large muscovite flakes ($K_2O = 8.48–10.95$ wt.%) (Table S2). These composition characteristics agree with the x-ray K mapping results where large muscovite flakes showed the highest K intensities while the sericite domains, in particular the low-K sericites, exhibited low to intermediate K intensities (Fig. S1). Some chlorite and minor silicic Ca-rich crystallites (CaO up to 8.37 wt.%) with K_2O contents (<0.36 wt.%) much lower than the muscovites and sericites are also present in the three andalusite crystals (Fig. 5b–c and e, Table S2). These results collectively suggest that large muscovite flakes and sericite aggregates along micro-cracks are the main K-bearing solid phases in the andalusite samples. Additionally, millimeter- to centimeter-scale thin transitional zones usually develop along the contact between quartz veins and host micaschists, where biotites are choritized (Fig. 5f).

4.3. Fluid inclusion characteristics

In most metamorphic rocks and veins, fluids are generally transported along mineral cracks. Repeated fissuring and healing is likely the most common and, in many cases, the only way to capture fluid inclusions (Crawford and Hollister, 1986; Boullier, 1999). The fluid inclusion planes

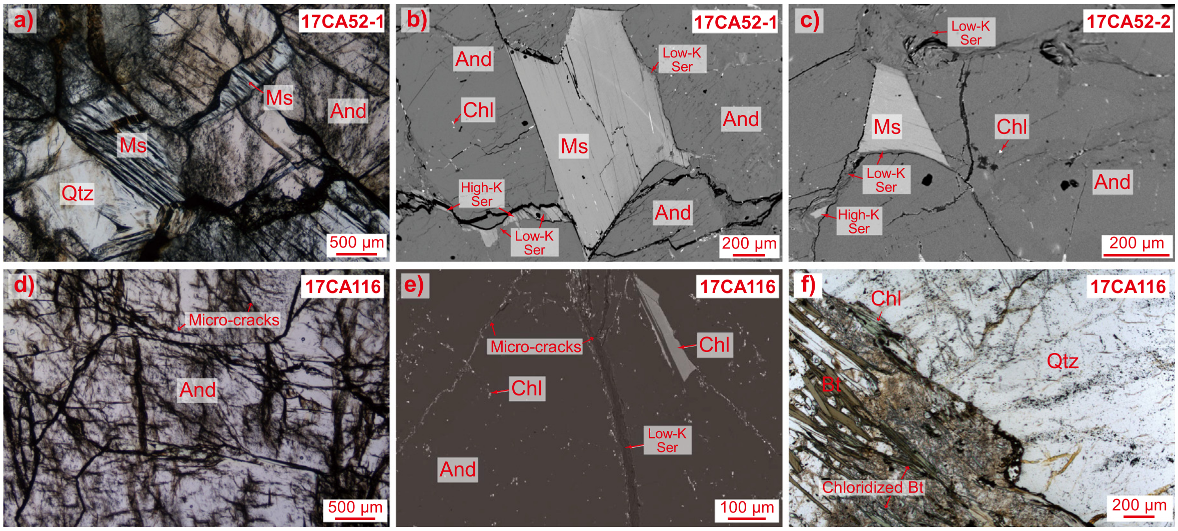

Fig. 5. Photomicrographs showing intergrown minerals in syn-tectonic veins and mineral impurities in andalusites. (a–e) Large muscovite flakes or fine-grained sericite aggregates in andalusite crystals. (f) Chloridized biotite at the contact of the quartz vein and wall rocks. Figures b, c and e are back-scattered electron (BSE) images. Qtz-quartz, Ms-muscovite, Ser-sericite, and Chl-chlorite.

(FIPs), formed from the healing of open cracks and indicate pathways and propagation directions of fossil fluids, can be used to determine regional paleostress histories and date related tectonic events (Boullier, 1999; Lespinasse, 1999; Siebenaller et al., 2016).

In the studied samples, fluid inclusions are very small (generally less than 5 μm with a few reaching 7 μm in diameter, Fig. 6), which makes microthermometric studies and *in-situ* compositional analyses difficult. These fluid inclusions are always found in planes and only one generation of FIPs was recognized (Fig. 6). These FIPs are oriented similarly from grain to grain and most of them do not cross grain boundaries (Fig. 6a–e). These characteristics suggest that these fluid inclusions are pseudosecondary rather than secondary. The growth of the andalusite was accompanied by vein formation during the regional D3 folding event, which resulted in a large number of intra-crystal fissures in the growing andalusite. During D3, syn-tectonic fluids migrating along fissures were preserved as FIPs during healing.

Fluid inclusions in the FIPs are mainly liquid-rich two-phase with relatively low vapor-filling degrees (generally less than 20%, Fig. 6b–e). Minor gas inclusions are also present in some FIPs (e.g., Fig. 6d). These fluid inclusions range from subspherical to irregular or elongated in shape (Fig. 6b–e). Some pure gas SFIs with sizes varying from several micrometers to nanometers are also present in the studied andalusite samples (Fig. 6f) while the liquid-rich SFIs are limited (Fig. 6).

5. ^{40}AR/^{39}AR DATING OF ANDALUSITE AND K-BEARING SOLID PHASES

5.1. Analytical methods

The above three andalusite mineral samples (17CA52-1, 17CA52-2, and 17CA116) were selected for fluid inclusion ^{40}Ar/^{39}Ar stepwise crushing experiments and two of the crushed residues (17CA52-1 and 17CA116, termed crushed powders in the following texts) were further measured by stepwise heating experiments using a furnace. Muscovite flakes extracted from andalusite crystals 17CA52-1 and 17CA52-2 and biotites extracted from the contact between the quartz vein of andalusite sample 17CA116 and its host rock were further analyzed using laser stepwise heating.

Large andalusite crystals were mechanically crushed and sieved. The andalusite fragments, muscovite flakes, and biotites were carefully hand-picked from the 250–830 μm fraction under a binocular microscope, which were rinsed several times with diluted nitric acid followed by deionized water in an ultrasonic bath to remove surface organics. Dried mineral samples (approximately 150 mg for each andalusite sample) were wrapped with aluminum foil and placed in aluminum vessels together with the biotite monitor standard ZBH-2506 which has a ^{40}Ar/^{39}Ar plateau age of 132.7 ± 0.1 Ma (1σ, Wang, 1983). The ZBH-2506 standard was co-irradiated between every two to four samples for *J*-value calculation. It has been experimentally confirmed that the recoil effects of ^{39}Ar could be negligible when the irradiated minerals have sizes above 100 μm (e.g., Ren and Vasconcelos, 2019). The relatively large grain sizes (>250 μm) of the studied minerals minimize the risk of ^{39}Ar loss through recoil during irradiation and hence such effect is not discussed in the current study.

Stepwise crushing of the irradiated andalusite samples and subsequent stepwise heating of the crushed powders were conducted at the MOE Key Laboratory of Tectonics and Petroleum Resources, China University of Geosciences (CUG). The stepwise crushing experiments were conducted using an *in-house* designed crushing system (Qiu and Jiang, 2007; Qiu et al., 2011). This system consists of a crushing tube (316L type stainless steel, length: 160 mm, inner diameter: 28 mm) with a spherical curvature on the internal base and a magnetic pestle (3Cr13 type (or S42030) stainless steel, weight: *ca.* 214 g). The magnetic pestle also has a spherical bottom which permits an appropriate match between the pestle and the crushing tube with a spherical curvature on the internal base. An adjustable repeating-timer-relay was used to repeatedly lift and drop the pestle from a height of 3–4 cm to crush the mineral samples at the bottom of the crushing tube by controlling an external electric magnet with a frequency of 2.5 Hz. Lateral crushing, achieved by two smaller pestles on the side wall of the bottom of the crushing tube, was applied after every drop of the pestle to prevent grains/powders from sticking to the tube and to homogeneously crush the samples.

In this study, the andalusite samples were crushed around twenty steps to fully release the gases in the fluid inclusions. The drop numbers of each crushing step were adjusted to maintain applicable gas levels for precise measurements. After the stepwise crushing experiments, the crushed powders were further analyzed for stepwise heating by placing the crush tube into a furnace. Around twenty heating steps were adopted to release the gases hosted by the solid phases with the heating temperatures gradually increasing from 200 °C to 800 °C. Heating at higher temperatures was avoided in the experiments due to very high blanks caused by degassing of the metal crushing tube. Released gases from crushing and heating were analyzed by an ARGUS VI® mass spectrometer. The mass spectrometer is equipped with one compact discrete dynode (CDD) ion counting multiplier and five Faradays that incorporate new high gain amplifier circuits with measuring resistors of 10^{-10}–10^{-13} Ω. The five argon isotopes (masses 40, 39, 38, 37, and 36) can be measured simultaneously by the five Faradays. Prior to analyses, the crushing or heating system was first baked out at 150 °C to achieve a low system blank. Blank measurements were carried out between every 3 to 4 sample analyses. The released gases were first cleaned with a cryotrap at −110 °C, followed by equilibration with a SAES ST101® Zr/Al getter at room temperature and another Zr/Al getter at 400 °C. The purification time is 400 s in total. The analytical procedures are the same as those described in Bai et al. (2018).

^{40}Ar/^{39}Ar laser stepwise heating of the remaining muscovite and biotite samples was conducted at State Key Laboratory of Isotope Geochemistry, Guangzhou Institute of Geochemistry, Chinese Academy of Sciences (GIG-CAS). The samples were heated using a 50 W CO_2 laser (10.6 mm) in ten more steps. The heating time of each step

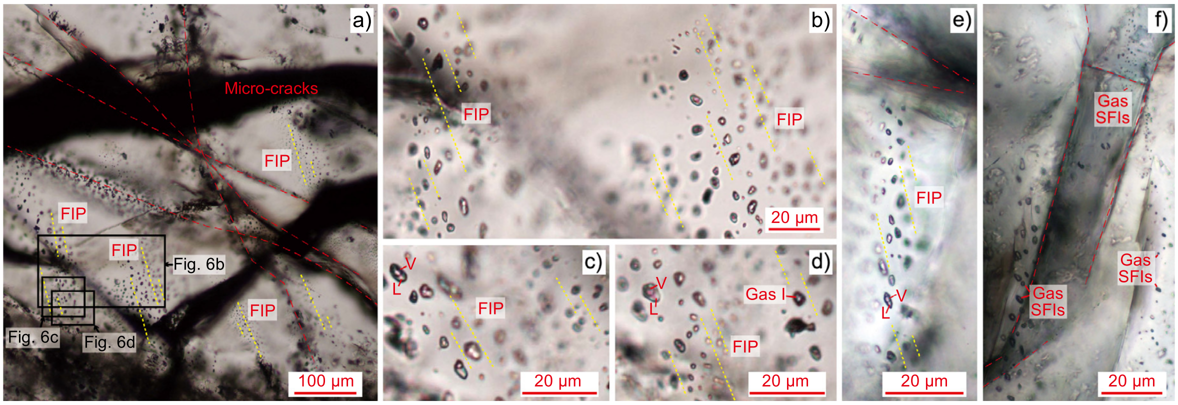

Fig. 6. Examples of fluid inclusions within andalusite crystals. FIP, Gas I, SFI, L, and V represent the fluid inclusion plane, gas inclusion, secondary fluid inclusion, liquid phase, and vapor phase, respectively. The major mineral micro-cracks are labeled by red dashed lines and the FIPs are indicated by yellow dashed lines. Note the abundant mineral impurities in the mineral micro-cracks.

was 60 s. The purification and analytical procedures of the released gases are similar to those in the CUG lab using similar Zr/Al getters and ARGUS VI® mass spectrometer, respectively. Detailed analytical procedures were described in Zhang et al. (2021).

The total decay constant for ^{40}K uses $\lambda = 5.543 \times 10^{-10}$/yr from Steiger and Jäger (1977). The modern atmospheric ^{40}Ar/^{36}Ar value used for the calculation of radiogenic argon (^{40}Ar*) is 298.56 from Lee et al. (2006). Uncertainties of the ^{40}Ar/^{39}Ar ages were reported at the 2σ level. In this study, at least 5 or more consecutive steps (consistent at 95% confidence level) that contain >70%, 50–70%, and <50% of the cumulative ^{39}Ar released were used to define a plateau, mini-plateau, and pseudo-plateau, respectively (see Hénocque et al., 1998; Jourdan et al., 2007; Schaen et al., 2021). Pseudo-plateau ages are particularly important in fluid inclusion ^{40}Ar/^{39}Ar geochronology. Given that the stepwise crushing process progressively extracts gases from the SFIs and PFIs, in most cases, degassing of PFIs could only form pseudo-plateau instead of typical plateau or mini-plateau ages (Qiu and Jiang, 2007; Jiang et al., 2012; Xiao et al., 2019). Detailed data and metadata of ^{40}Ar/^{39}Ar geochronology are presented in Tables S3–S6.

5.2. ^{40}Ar/^{39}Ar stepwise crushing

The gases extracted from the ^{40}Ar/^{39}Ar stepwise crushing experiments of the three andalusite samples (17CA52-1, 17CA52-2, and 17CA116) are characterized by relatively high ^{40}Ar*, ^{38}Ar$_{Cl}$, and low ^{39}Ar$_K$ intensities with high ^{40}Ar*/^{39}Ar$_K$, ^{38}Ar$_{Cl}$/^{39}Ar$_K$, and variable K/Ca ratios in the first several to tens of crushing steps (Tables S3–S4). These steps yielded similar decreasing staircase-shaped age spectra with old apparent ages (Fig. 7a, c and e). The following crushing steps yielded less variable K/Ca and relatively low ^{40}Ar*/^{39}Ar$_K$ and ^{38}Ar$_{Cl}$/^{39}Ar$_K$ ratios (Tables S3–S4) and formed different ^{40}Ar/^{39}Ar age spectra (Fig. 7a, c and e). Sample 17CA52-1 yielded a flat age spectrum in crushing steps 9–16 defining a pseudo-plateau age of 278.2 ± 2.7 Ma (MSWD = 0.1), which is followed by an increasing staircase-shaped age spectrum in crushing steps 17–20 likely caused by the decreasing ^{39}Ar$_K$ contents (Fig. 7a, Table S3). Steps 9–16 also formed a well-defined inverse isochron with an isochron age of 277.2 ± 5.7 Ma (MSWD = 0.1) (Fig. 7b). The initial ^{40}Ar/^{36}Ar ratio of 299.9 ± 6.7 approximates the modern atmospheric ratio of 298.56 (Lee et al., 2006), indicating limited excess argon in the fluids. Samples 17CA52-2 and 17CA116 yielded similar increasing staircase-shaped age spectra and well-defined inverse isochrons in the last crushing steps with isochron ages of 277.2 ± 5.5 Ma (MSWD = 0.6, steps 13–22, Fig. 7d) and 282.2 ± 4.0 Ma (MSWD = 0.2, steps 13–19, Fig. 7f), respectively. The initial ^{40}Ar/^{36}Ar ratios for sample 17CA52-2 and sample 17CA116 are 451.6 ± 6.3 and 634.3 ± 9.8, respectively, which are higher than the atmospheric ratio indicating the presence of excess argon in the fluids. Assuming that the trapped excess argon has the ^{40}Ar/^{36}Ar ratio of 451.6 for sample 17CA52-2 and 634.3 for sample 17CA116, the last crushing steps yielded flat age spectra with pseudo-plateau ages of 277.2 ± 3.0 Ma (MSWD = 0.5) and 282.2 ± 2.8 Ma (MSWD = 0.2), respectively, which are in line with their respective inverse isochron ages (Fig. 7c–f).

Gases released during the last crushing steps of the three andalusite samples also exhibit good linear correlations on plots of ^{39}Ar$_K$/^{38}Ar$_{Cl}$ versus ^{40}Ar*/^{38}Ar$_{Cl}$ and display nearly constant ^{40}Ar*/^{39}Ar$_K$ ratios on plots of ^{39}Ar$_K$/^{40}Ar* versus ^{38}Ar$_{Cl}$/^{40}Ar* and ^{38}Ar$_{Cl}$/^{39}Ar$_K$ versus ^{40}Ar*/^{39}Ar$_K$ (Fig. S2). Ages calculated from the slopes of the regression lines and average ^{40}Ar*/^{39}Ar$_K$ ratios in the Cl–K–Ar correlation diagrams are 278 Ma, 277 Ma, and 282 Ma for samples 17CA52-1, 17CA52-2, and 17CA116, respectively (Fig. S2).

5.3. ^{40}Ar/^{39}Ar stepwise heating

Micron-sized crushed andalusite powders of samples 17CA52-1 and 17CA116 were further analyzed using the ^{40}Ar/^{39}Ar stepwise heating technique. Stepwise heating of powdered sample 17CA52-1 yielded a discordant age spectrum with very young apparent ages from 27.5 to 179.4 Ma that failed to define a plateau (Fig. 8a). Data points of this

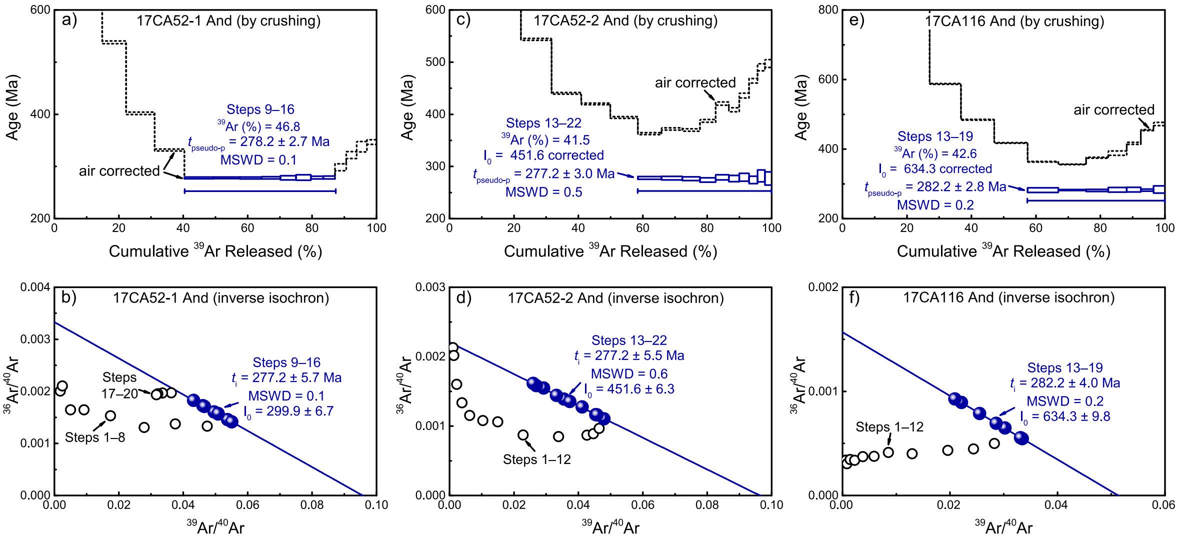

Fig. 7. Fluid inclusion $^{40}Ar/^{39}Ar$ ages of andalusite samples by stepwise crushing. The pseudo-plateau ages ($t_{pseudo\text{-}p}$, solid blue lines) were calculated by assuming trapped initial $^{40}Ar/^{36}Ar$ ratios (I_0) of 298.6 (air ratio), 451.6, and 634.3, respectively. The black dashed lines in Figures a, c and e represent air ratio (298.6) corrected age spectra. The error ellipses are presented in the inverse isochron diagrams.

sample scatter in the inverse isochron plot and fail to form an isochron (Fig. S3a). The released gases also show large $^{38}Ar_{Cl}/^{39}Ar_K$ and $^{37}Ar_{Ca}/^{39}Ar_K$ compositional variations at different heating temperatures (Fig. 8b–c). It is noteworthy that a considerable amount of $^{39}Ar_K$ was released during the last heating steps of powdered sample 17CA52-1 (Table S5), implying that some argon gases likely remain in the sample and additional heating steps at higher heating temperatures could generate higher apparent ages. Stepwise heating of the powdered sample 17CA116 yielded an increasing staircase-shaped age spectrum (Fig. 8d) but a well-defined inverse isochron (Fig. S3b) in steps 3–20. The inverse isochron gave an age of 216.2 ± 3.9 Ma (MSWD = 0.2) and an initial $^{40}Ar/^{36}Ar$ ratio of 304.0 ± 1.3 (Fig. S3b), indicating the presence of minor excess argon. Assuming that the trapped argon has the $^{40}Ar/^{36}Ar$ ratio of 304.0, these steps yielded a plateau age of 216.2 ± 2.7 Ma (MSWD = 0.2) (Fig. 8d). Unlike the powdered sample 17CA52-1, the amount of $^{39}Ar_K$ in this sample decreased significantly in the last heating steps (Table S5), which suggests effective extraction of Ar reservoirs in the powders. The released gases show relatively uniform $^{38}Ar_{Cl}/^{39}Ar_K$ ratios but variable $^{37}Ar_{Ca}/^{39}Ar_K$ ratios at different heating temperatures (Fig. 8e–f).

Laser stepwise heating of muscovite flakes selected from the andalusite samples 17CA52-1 and 17CA52-2 yielded a mini-plateau age of 243.4 ± 2.3 Ma (MSWD = 1.0, accounting for 54.4% of the released ^{39}Ar) and a well-defined plateau age 240.6 ± 2.3 Ma (MSWD = 0.9, accounting for 100% of the released ^{39}Ar), respectively (Fig. 8g–h). These ages agree with their inverse isochron ages (Fig. S3c–d). Laser stepwise heating of biotite sample 17CA116 yielded a discordant age spectrum with a mini-plateau age of 213.5 ± 2.0 Ma (MSWD = 1.2, accounting for 52.6% of the released ^{39}Ar) in steps 11–20 (Fig. 8i). These points also formed an inverse isochron with an age of 213.6 ± 3.0 Ma (MSWD = 1.4) (Fig. S3e). The biotite age approximates the stepwise heating age of the crushed powder of the associated andalusite sample (Fig. 8d).

6. MONAZITE U–PB DATING

6.1. Analytical methods

Monazites from two leucogranite dykes 17CA118 and 17CA128 that intrude the migmatite-granite complex were analyzed for U–Pb geochronology. These dykes were initially emplaced nearly perpendicular to regional NW-SE striking S3 foliation and slightly folded by the ongoing D3 event (Fig. 3a–c), which indicates syn-tectonic emplacement. Their ages can therefore be used to evaluate the accuracy of the andalusite fluid inclusion $^{40}Ar/^{39}Ar$ ages.

Monazite LA-ICP-MS U–Pb dating was conducted using a GeolasPro laser ablation system coupled with an Agilent 7700e ICM-MS instrument at the Wuhan SampleSolution Analytical Technology Co., Ltd., Wuhan, China. The analysis was performed with a beam diameter of 16 μm. Monazite standard 44069 with a recommended age of 424.9 ± 2.4 Ma (by ID-TIMS, Aleinikoff et al., 2006) was used as the external standard. Each analysis includes a background acquisition of *ca.* 25–30 s followed by data acquisition of 65 s. The analytical procedures used were the same as those described by Zong et al. (2017). Mass fractionation correction and calculation were processed by the software ICPMSDataCal (Liu et al., 2008). Weighted mean $^{206}Pb/^{238}U$ ages are reported at 2σ level. Data reduction and calculation were carried out using the Isoplot/Exv. 3.75 program (Ludwig, 2001). The results are presented in Table S7.

6.2. Results

The monazite grains of sample 17CA118 are euhedral to subhedral and stubby to equant. Most grains are

50–150 μm in length with the length/width ratios varying from 1:1 to 1:2. Back-scattered electron (BSE) images show that most monazite grains have relatively homogenous structures, some grains contain substantial mineral inclusions, and a few grains show patchy zonation (Fig. 9a). Twenty-nine grains yielded $^{206}Pb/^{238}U$ ages ranging from 278.8 to 266.9 Ma with a weighted mean age of 272.8 ± 1.1 Ma (MSWD = 1.5) (Fig. 9a).

Monazite grains of sample 17CA128 are subhedral grains varying from 20 to 200 μm in length with the length/width ratios ranging from 1:1 to 1:4. Most grains have minor mineral inclusions and display unzoned internal structures in BSE images (Fig. 9b). Twenty-one grains yielded $^{206}Pb/^{238}U$ ages ranging from 280.8 to 271.6 Ma with a weighted mean age of 275.1 ± 1.2 Ma (MSWD = 1.4) (Fig. 9b).

7. DISCUSSION

7.1. The significance of $^{40}Ar/^{39}Ar$ ages

7.1.1. 282–277 Ma from stepwise crushing of andalusites

It has been documented that the gentle stepwise crushing technique can preferentially extract gases from larger and irregular SFIs in the first crushing steps and allow the release of the smaller and liquid-rich PFIs in the last crushing steps (e.g., Qiu and Wijbrans, 2006; Qiu and Jiang, 2007; Jiang et al., 2012; Bai et al., 2013; Xiao et al., 2019).

Gases extracted from the first crushing steps of the three andalusite samples are characterized by very high $^{40}Ar^{*}/^{39}Ar_K$ ratios (Fig. S2, Table S3), which likely came from K-poor and ^{40}Ar-rich gas sources. As mineral grains would preferentially breakup along micro-cracks, secondary gases trapped along micro-cracks would be extracted first. Additionally, gas SFIs are also present in andalusite crystals (Fig. 6f). This type of inclusion has much lower densities compared to the liquid-rich fluid inclusions and could therefore also be extracted in the first crushing steps (see the summary of Xiao et al. (2019, 2022)).

During the following crushing steps, the three andalusite samples yielded regular, predictable age spectra, well-constrained isochrons, nearly identical $^{40}Ar^{*}/^{39}Ar_K$ ratios as well as consistent pseudo-plateau and isochron ages of 282–277 Ma (Fig. 7 and Fig. S2). These observations suggest that most of the secondary gases were released in the first crushing steps and the last crushing steps mainly extracted gases from the smaller intra-crystal liquid-rich FIPs (Fig. 6). Therefore, these ages are likely geologically

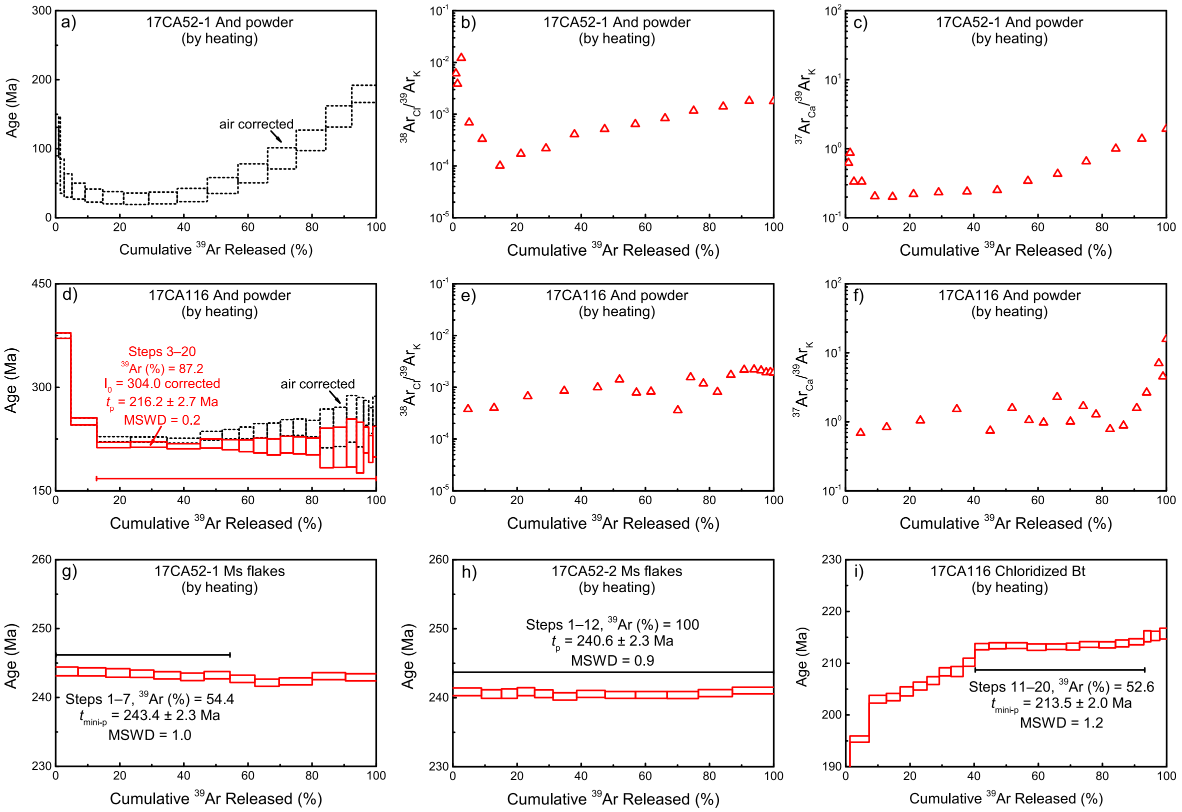

Fig. 8. Stepwise heating $^{40}Ar/^{39}Ar$ results of crushed andalusite powders (a–f), muscovite flakes in andalusites (g–h), and biotite in the margin of the quartz vein (i). The black dashed lines in Figures a and d represent air ratio (298.6) corrected age spectra. The plateau (t_p) or mini-plateau ($t_{mini\text{-}p}$) ages (solid red lines) in Figures d and g–i were calculated by assuming trapped initial $^{40}Ar/^{36}Ar$ ratios (I_0) of 304.0 and 298.6, respectively. The respective inverse isochrons are presented in Fig. S3.

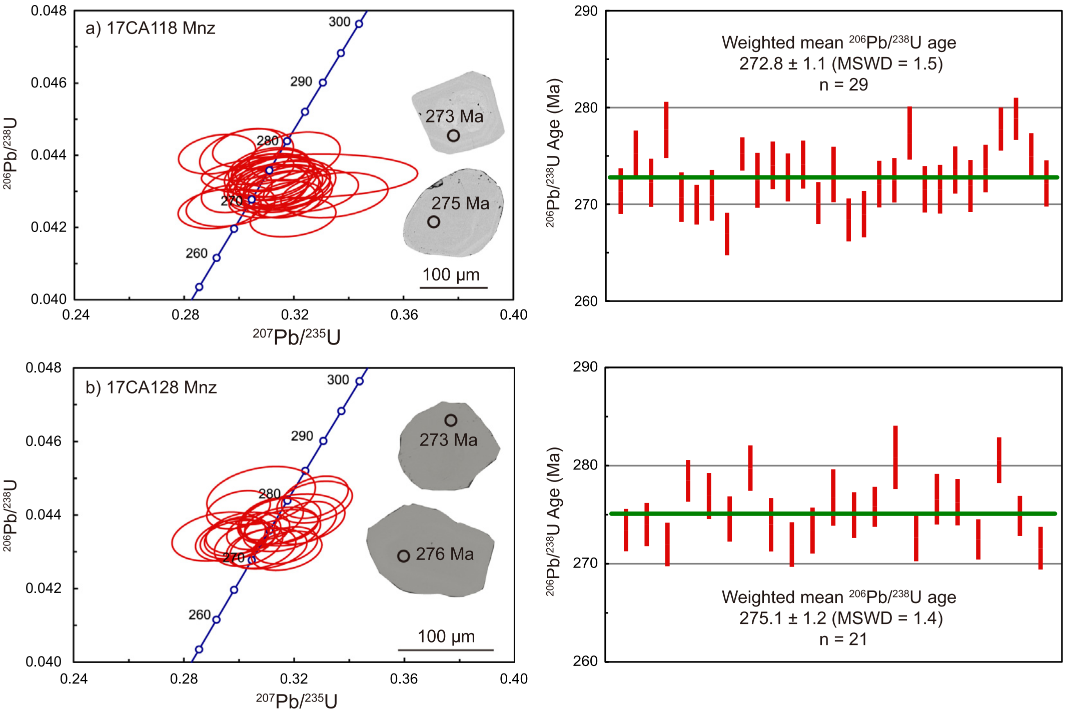

Fig. 9. U–Pb concordia diagrams and weighted mean ages for monazites from syn-tectonic leucogranite dykes.

significant and correspond to the formation age of the FIPs and the host andalusites.

7.1.2. 243–241 Ma from laser stepwise heating of muscovite flakes

Muscovite flakes associated with andalusite samples 17CA52-1 and 17CA52-2 yielded nearly identical ages of 243–241 Ma. These ages are much younger than the ^{40}Ar/^{39}Ar ages (282–277 Ma) from the last crushing steps of andalusite crushing experiments, the crystallization ages (280–273 Ma) of syn-D3 pegmatites and leucogranites (zircon/monazite U–Pb, Jiang et al., 2019 and this study), and the metamorphic ages of the host micaschists (279–262 Ma, monazite U–Pb, Jiang et al., 2021b). Therefore, it is very unlikely that the muscovite ^{40}Ar/^{39}Ar ages date the same event as the andalusite fluid inclusion ^{40}Ar/^{39}Ar ages.

Many ^{40}Ar/^{39}Ar studies on metamorphic white micas have highlighted that volume diffusion of Ar may have a subordinate effect on ^{40}Ar/^{39}Ar ages of white micas compared with recrystallization (Di Vincenzo et al., 2001, 2004; Villa et al., 2014; Villa, 2016; Bosse and Villa, 2019). Stepwise heating mixtures of multiple mica generations should cause significant discordance of the ^{40}Ar/^{39}Ar age spectra (Di Vincenzo et al., 2004; Villa et al., 2014; Villa and Hanchar, 2017). As revealed by petrographic observations, the dated muscovite minerals are coarse-grained, euhedral crystals that display equilibrium textures with the associated andalusites (Fig. 5a–c). These features indicate that the muscovite did not recrystallize in a subsequent tectono-metamorphic event. Although minor sericite alterations (dominated by low-K sericites) occur along the margins or fractures of the large muscovite flakes (Fig. 5b–c), their identical K/Cl (189.6–192.8 for sample 17CA52-1 and 184.2–189.1 for sample 17CA52-2) and very low Ca/K (near 0) ratios (Figs. S4–S5, Table S6) suggest that the gases were mainly derived from large muscovite flakes (CaO near 0) and the effects of the low-K sericites (CaO up to 1.22 wt.%, Table S2) are negligible.

Instead, these young muscovite ^{40}Ar/^{39}Ar ages likely record cooling of the quartz veins. Recent metamorphic pressure–temperature investigations on the host micaschists suggested that andalusites grew at metamorphic temperature conditions of 550–600 °C (Jiang et al., 2021b), which is much higher than the reported T_C for muscovite, e.g., 425 °C (Harrison et al., 2009). This implies that the muscovite K/Ar clock was set during the cooling stage rather than the growth stage of andalusites. Notably, the generated ^{40}Ar/^{39}Ar ages broadly overlap with many published mica ^{40}Ar/^{39}Ar ages of 250–240 Ma from the micaschists and/or paragneisses along the southern Chinese Altai, which were considered as the timing of the regional uplift and cooling (Laurent-Charvet et al., 2003; Briggs et al., 2009).

7.1.3. 216–214 Ma from stepwise heating of andalusite powder and chloridized biotite

The andalusite minerals contain very little K in their lattice positions (0 to tens of ppm, Table S1). Heating experiments on crushed andalusite powders, in theory, would extract K (Ar) from the remaining fluid inclusions as well as any K-bearing mineral impurities (e.g., Qiu and Jiang, 2007; Hu et al., 2015). The presence of K-rich impurities such as sericites (K_2O contents can be up to 8.48 wt.% in our andalusites, Table S2) would exert an important influence on the heating ages of K-poor minerals (Villa et al., 1996; Verati and Jourdan, 2014; Jiang et al., 2021a).

The dated andalusite samples contain different mineral impurities. For example, andalusite sample 17CA52-1 contains abundant muscovite flakes and high-K sericites whereas those impurities are much less apparent in sample 17CA116 (Fig. 5a–e). Nevertheless, low-K sericites and chlorite widely occur in micro-cracks in both samples (Fig. 5b–e). In addition, minor Ca-rich silicic microlites are also present in these minerals (Table S2). Therefore, the major solid-phase K reservoirs in andalusite powder 17CA52-1 are muscovite flakes, high-K and low-K sericites whereas those in andalusite sample 17CA116 are merely low-K sericites. These discrepancies regarding compositions of mineral impurities may explain the different results of their heating experiments. Stepwise heating of the crushed andalusite powder 17CA52-1 exhibited highly varied Cl–K–Ca–Ar elemental and isotopic compositions at different heating temperatures (Fig. 8b–c, Fig. 10a and c, and Figs. S6–S7), which implies degassing from diverse sources (i.e., different K- and Ca-bearing impurities) during heating. Consequently, such mixed gases led to discordant and geological meaningless ages (Fig. 8a). In contrast, gases released from sample 17CA116 show less variable Cl–K–Ca–Ar elemental and isotopic compositions (Fig. 8e–f, Fig. 10b and d, and Figs. S6–S7). These gases formed a relatively flat age spectrum (Fig. 8d) and well-defined inverse isochron with an age of *ca.* 216 Ma (Fig. S3b), which should be geologically meaningful and correspond to secondary alteration.

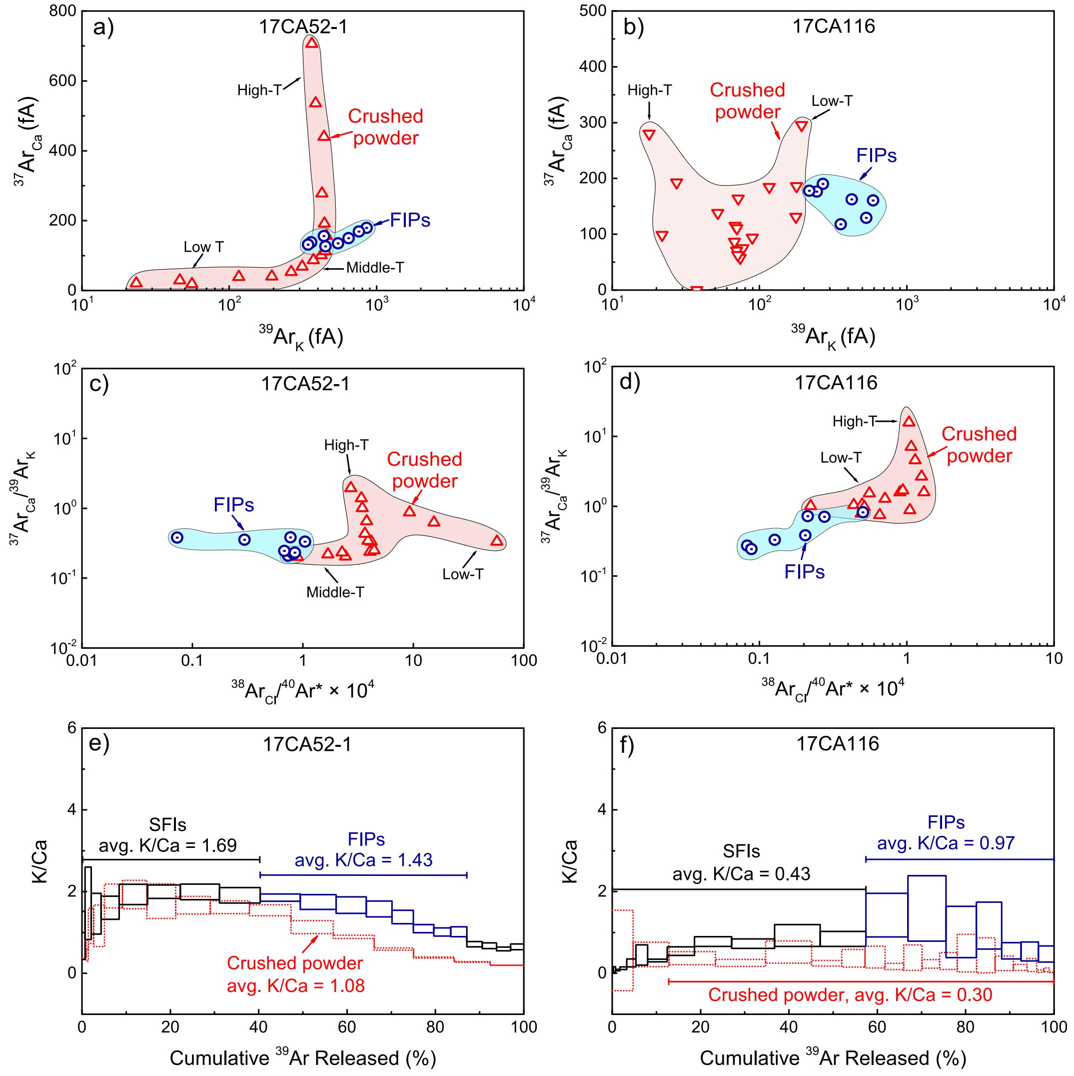

Fig. 10. Comparison of K–Ca–Cl–Ar correlations of the crushing and heating experiments. (a, b) Plots of $^{39}Ar_K$ versus $^{37}Ar_{Ca}$ contents. (c, d) Plots of $^{38}Ar_{Cl}/^{40}Ar^*$ versus $^{37}Ar_{Ca}/^{39}Ar_K$ ratios. Gases released in the low- (low-T), middle- (middle-T), and high-temperature (high-T) stages during stepwise heating of the crushed andalusite powders are labeled in the figures. Data from steps 1–2 of the andalusite powder 17CA116 by stepwise heating were excluded in age calculation and thus were not shown in these plots. (e, f) K–Ca spectra. Average K/Ca ratios of different gas sources are indicated.

Laser stepwise heating on the chloridized biotite sample 17CA116 gave an age of *ca.* 214 Ma (Fig. 8i). This age is near-identical to that of the crushed andalusite powder 17CA116 that displayed sericite and chlorite alteration (Fig. 8d). These *ca.* 216–214 Ma ages probably reflect the timing of a late hydrothermal alteration event in the region. It is noteworthy that a small granitic pluton (the Shangkelan granite) located about 20 km to the northeast was dated at *ca.* 209 Ma (e.g., Lin et al., 2019). Minor granitic intrusions and pegmatites of similar ages (e.g., 220–209 Ma) were also present in the southern Chinese Altai (Wang et al., 2007; Liu et al., 2014; Wang et al., 2014a; Lin et al., 2019). It is therefore most likely that the regional Late Triassic magmatism caused the *ca.* 216–214 Ma secondary hydrothermal perturbation in the study area. Given the relatively weak alteration present in the andalusite crystals and the uniform ages from their crushing experiments, the effects of the hydrothermal perturbation on the pre-existing FIPs should be limited.

7.2. Limited interference from solid K-bearing phases to the FIP ages

In this investigation, K-bearing solid phases occur in the andalusite samples as large muscovite flakes, and as sericite aggregates and chlorites along mineral margins or micro-cracks (Fig. 5a–e and Fig. S1). An important question is whether gases from these K-bearing minerals were released during gentle stepwise crushing of andalusite. The distinct ages and compositional characteristics between the crushing and heating experiments in this study provide important evidence that gases in solid phases are not released during the gentle stepwise crushing, which has been shown by other studies as well (Jiang et al., 2012; Bai et al., 2013; Xiao et al., 2019).

Heating of powdered sample 17CA52-1 failed to form an age plateau (Fig. 8a) while that of powdered sample 17CA116 yielded an age of *ca.* 216 Ma (Fig. 8d). Laser stepwise heating of muscovite flakes selected from samples 17CA52-1 and 17CA52-2 yielded consistent $^{40}Ar/^{39}Ar$ ages of 243–241 Ma (Fig. 8g–h). These ages are all younger than the stepwise crushing $^{40}Ar/^{39}Ar$ ages of *ca.* 282–277 Ma of the three andalusite samples (Fig. 7). The large differences in these $^{40}Ar/^{39}Ar$ ages suggest that there was limited K (Ar) interference from K-bearing solid phases to the FIP ages generated by gentle stepwise crushing.

Apart from the differences in the apparent ages, gases released from the crushing and heating experiments also show different chemical characteristics in $^{39}Ar_K$–$^{37}Ar_{Ca}$ and $^{38}Ar_{Cl}/^{40}Ar^*$–$^{37}Ar_{Ca}/^{39}Ar_K$ diagrams and display different K–Ca spectra (Fig. 10). For example, FIP-related gases from the andalusite sample 17CA52-1 show $^{38}Ar_{Cl}/^{40}Ar^*$ ratios that are an order of magnitude lower than those of gases from heating of the crushed powder (Fig. 10c, Tables S4–S5). FIP-related gases from the andalusite sample 17CA116 have lower $^{37}Ar_{Ca}/^{39}Ar_K$ (Fig. 10d) and elevated K/Ca spectrum (K/Ca = 0.47–1.59, Table S3) than those of gases from the heating experiment carried out on its crushed powder (K/Ca = 0.02–0.52, Table S5) (Fig. 10f). More importantly, the stepwise heating experiment on the crushed powder of this sample yielded near atmospheric initial $^{40}Ar/^{36}Ar$ ratio of 304.0 (Fig. 8d), indicating insignificant excess argon in the solid phases. This is distinct from the FIPs which yielded an initial $^{40}Ar/^{36}Ar$ ratio of 634.3 (Fig. 7f). Additionally, gases from the FIPs also show much smaller compositional variations compared with those released by the heating experiments from the andalusite powders (Fig. 10a–d). These lines of evidence further support the notion that gases extracted during the crushing and heating experiments come from distinct reservoirs.

7.3. Cl–K–Ca–Ar correlations and implications

7.3.1. Origins and hydrothermal processes of the FIPs

Degassing of FIPs from the three andalusite samples yielded consistent ages (Fig. 7) indicating that they dated the same hydrothermal event. However, the related argon gases show distinct features in their Cl–K–Ca–Ar correlations (Figs. S4–S6). One possible reason is that the original fluids were derived from different devolatilization reactions of surrounding metamorphic rocks. Based on fluid inclusion analysis of fissure veins hosted by different metamorphic rocks in the Central Alps, Rauchenstein-Martinek et al. (2016) showed that the metamorphic fluids exhibited variable K and Ca contents with K/Ca ratios ranging from 0 to several hundreds. Even in the same fluid inclusion assemblage (FIA) that represents a separate fluid event during the evolution of a mineral (Goldstein and Reynolds, 1994), the Ca and K contents can vary across several orders of magnitude (Rauchenstein-Martinek et al., 2016). In this study, the host rocks of the quartz veins are metamorphosed Habahe Group rocks that are considered originally Ordovician accretionary wedge sediments, typically of diverse chemical compositions (Long et al., 2008). The heterogeneous Ca/K and Cl/K ratios of the FIPs in the studied andalusite samples (Fig. 10 and Figs. S4–S6) probably reflect different compositions of the host rocks. Besides, different degrees of fluid-wall rock interactions would also cause different compositional features in the evolved fluids. This mechanism may explain why FIPs in andalusites from the margins of the quartz veins show different K/Ca ranges (sample 17CA52-2: 0.02–0.87, sample 17CA116: 0.47–1.59, Table S3) from the andalusite from the center of the vein (sample 17CA52-1: 1.01–1.85, Table S3). The latter likely experienced less extensive fluid-wall rock interactions.

On the other hand, minor tiny SFIs (a few micrometers to nanometers, e.g., Fig. 6f) are also present in the andalusite crystals with abundances varying from sample to sample and even from grain to grain. Tiny fluid inclusions in metamorphic minerals usually have distinct compositions from the larger PFIs (Bodnar and Samson, 2003). They can sustain larger internal pressures and could be extracted in the last several crushing steps together with the small liquid-rich PFIs (Xiao et al., 2019, 2022), for example, the FIPs in this study, which may contribute to the different Ar compositions and age spectra observed in the last several crushing steps (Fig. 7).

7.3.2. Preservation of excess ^{40}Ar in K-poor metamorphic minerals

The current stepwise crushing experiments yielded saddle-shaped age spectra (Fig. 7a, c and e), indicating the presence of excess argon. Similar age spectra were reported from many previous ^{40}Ar/^{39}Ar experiments, in particular, on low-K and K-poor minerals such as amphibole, tourmaline, and quartz (e.g., Kelley, 2002; Barredo et al., 2009; Hu et al., 2018). These studies proposed that the excess ^{40}Ar were captured in variable positions, including mineral lattices, crystal channels, grain margins, and/or mineral-hosted fluid/melt inclusions (Kelley, 2002; Qiu and Wijbrans, 2006; Qiu et al., 2007; Hu et al., 2018).

In this work, abnormally old apparent ages alongside large amounts of excess ^{40}Ar occur primarily in the initial crushing stages (Fig. 7), which is interpreted as degassing mainly from the large pure gas SFIs (e.g., Fig. 6f). The subsequently extracted liquid-rich FIPs contain variable but lower excess ^{40}Ar based on their initial ^{40}Ar/^{36}Ar ratios (299.9, 451.6, and 634.3 for samples 17CA52-1, 17CA52-2, and 17CA116, respectively, Fig. 7b, d and f). In contrast, heating experiments on the crushed powders yielded either much younger apparent ^{40}Ar/^{39}Ar ages (Fig. 8a) or nearly atmospheric initial ^{40}Ar/^{36}Ar ratio (Fig. 8d). These features indicate that high excess ^{40}Ar was almost exhausted during the crushing experiments. In other words, the fluid inclusions, in particular the gas-rich ones, could serve as the main excess ^{40}Ar reservoirs in K-poor nesosilicate minerals. This is consistent with the earlier findings that Ar gases are preferentially partitioned into the vapor phases (Kelley, 2002).

In the study area, many andalusite-bearing HT/LP metamorphic domains developed in the vicinity of the syn-D3 dykes and andalusite-bearing quartz veins (Fig. 2b). Extensive circulation of hydrothermal fluids should have caused significant fluid-rock interactions with the host metamorphic Habahe Group rocks. Metamorphic investigations suggested that the regional HT/LP metamorphism developed at 3–5 kbar corresponding to a depth of 10–20 km (Wei et al., 2007; Jiang et al., 2021b). Metamorphic fluids may incorporate excess components from the surrounding rocks during circulation at such a depth (Turner and Wang, 1992; Kendrick and Burnard, 2013). However, such notion is not fully supported by findings from andalusite crushing that the FIPs-related gases in sample 17CA52-1 have an air-like initial ^{40}Ar/^{36}Ar ratio (Fig. 7b). Similar features were also reported from many hydrothermal ore systems from South China, where the PFIs usually contained very limited excess ^{40}Ar (Qiu and Jiang, 2007; Bai et al., 2013; Xiao et al., 2019; Bai et al., 2021). There, a relatively open environment was proposed for the circulation of hydrothermal fluids, which resulted in the escape of excess ^{40}Ar in the primary fluids (e.g., Bai et al., 2021). In the study area, meter-scale, thick and continuous quartz veins are present, implying circulation of metamorphic fluids probably in a similar open environment (e.g., Figs. 3–4). More importantly, the regional D3 event formed penetrative NW-trending subvertical S3 foliations (Fig. 2b) and fracture networks across the region, which could provide excellent chances for shallow components, e.g., meteoric water (Menzies et al., 2014; Dusséaux et al., 2019), to infiltrate to depth and excess components trapped in the deeply circulating fluids to escape away. Such formation environment might contribute to the escape of the excess ^{40}Ar from the primary fluids or partial equilibrium of the fluids with shallow components during the formation of andalusites, which could lead to their initial ^{40}Ar/^{36}Ar ratios close to, or nearly identical to the air ratio. In contrast, secondary fluids in association with later hydrothermal perturbations were captured by mineral micro-cracks in a relatively closed environment, which might better preserve excess ^{40}Ar (if any) in the fluids.

7.4. New perspective on dating regional deformation and metamorphism

Multiple lines of evidence suggest that ^{40}Ar/^{39}Ar stepwise crushing of andalusite indeed dates deformation and metamorphic events in the region. The formation ages of andalusites of 282–277 Ma inferred from the last steps of the gentle stepwise crushing experiments overlap with monazite U–Pb ages (275–273 Ma) of the syn-D3 leucogranite dykes (Fig. 9). These ^{40}Ar/^{39}Ar ages also agree very well with the 280–273 Ma zircon and monazite U–Pb ages of adjacent syn-tectonic granite intrusions and pegmatite dykes which are generally considered as the timing of regional D3 event in the study area (Fig. 11a, Jiang et al., 2019). Additionally, the andalusite-bearing HT/LP metamorphic domains developed in the vicinity of the syn-D3 dykes and veins in the study area. Metamorphic monazites included in andalusite minerals in the surrounding micaschists yielded U–Pb ages in the range of 279–269 Ma (Jiang et al., 2021b), which overlaps with the andalusite fluid inclusion ^{40}Ar/^{39}Ar ages (282–277 Ma) (Fig. 11a). More importantly, coeval HT/LP metamorphisms were prevailing along the southern Chinese Altai, as indicated by the occurrence of garnet-orthopyroxene-bearing granulites, cordierite-bearing migmatities, and andalusite-bearing micaschists in these regions (Wang et al., 2009; Li et al., 2014; Tong et al., 2014; Liu et al., 2019). The consistency between the andalusite fluid inclusion ^{40}Ar/^{39}Ar ages and the timing of HT/LP metamorphism recorded by U–Pb ages of zircon overgrowths from a nearby sillimanite-bearing paragneiss (299.2 ± 3.4 Ma, Wang et al., 2014b) as well as zircon/monazite U–Pb ages for granulites and migmatities in the neighboring regions (*ca.* 300–278 Ma, Wang et al., 2009; Tong et al., 2014; Broussolle et al., 2018) (Fig. 11) suggests that the formation ages of the syn-tectonic andalusites can also represent the time of contemporaneous metamorphism in this region.

In most metamorphic terranes worldwide, datable minerals such as zircons, monazites, garnets, and micas mainly form through partial melting and subsequent crystallization. However, partial melting is not common in many low- to medium-grade metamorphic terranes and metamorphic fluids commonly form quartz veins with limited datable materials. This challenge limits the scope of tectonothermal evolution studies. Andalusites are commonly present in quartz veins in low- to medium-grade metamorphic terranes, especially in metapelitic terranes (Whitney and

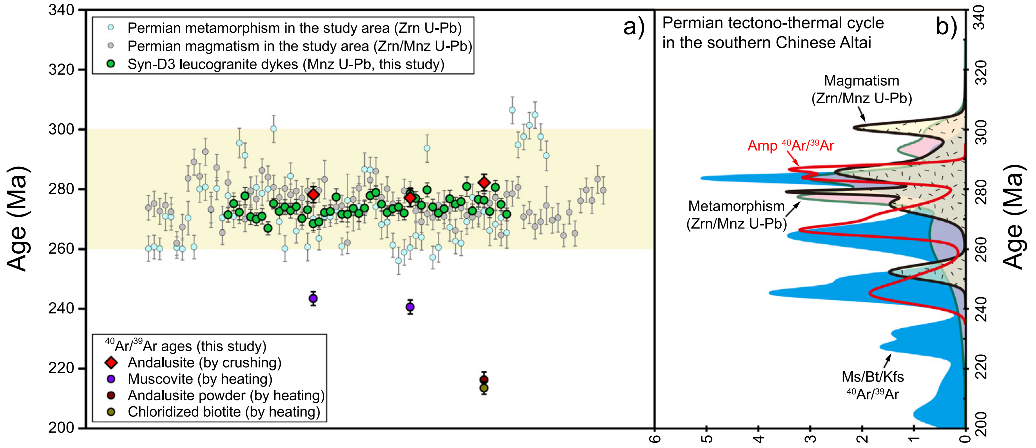

Fig. 11. Compilations of available ages for Permian tectono-thermal cycle in the study area (a) and the southern Chinese Altai (b). Age data of the study area are from the same sources for Fig. 2d. Age data of regional Permian magmatism and metamorphism in the southern Chinese Altai are magmatic zircon ages of granitoids and leucosome dykes from Zhang et al. (Zhang et al., 2012; Broussolle et al., 2018; Lin et al., 2019; Xu et al., 2021) and metamorphic zircon and monazite ages of gneisses and granulites from Zheng et al. (Zheng et al., 2007a; Wang et al., 2009; Li et al., 2014; Tong et al., 2014; Chen et al., 2019; Liu et al., 2020), respectively. ^{40}Ar/^{39}Ar ages are from Laurent-Charvet et al. (Laurent-Charvet et al., 2003; Briggs et al., 2007; Briggs et al., 2009; Li et al., 2015; Li et al., 2017). Amp-amphibole, Kfs-K-feldspar.

Dilek, 2000; Sepahi et al., 2004). Our results demonstrate that when accompanied by detailed petro-structural analyses, the newly established ^{40}Ar/^{39}Ar gentle stepwise crushing method of andalusite can be used to place age constraints on vein formation, and potentially, associated deformation and metamorphism, which opens up exciting new possibilities in tectonics and geochronology in general.

8. CONCLUSIONS

This study reports the first ^{40}Ar/^{39}Ar ages of fluid inclusion-bearing andalusites in syn-tectonic quartz veins from the Chinese Altai Orogen using the gentle stepwise crushing technique. Combined with refined structural analyses, EPMA mineral composition analyses, and monazite U–Pb geochronology, this study establishes fluid inclusion ^{40}Ar/^{39}Ar gentle stepwise crushing of andalusite as a reliable new method to date regional deformation and metamorphism. The main observations and conclusions are:

1) Andalusites in syn-tectonic quartz veins contain abundant intra-crystal planar fluid inclusions (FIPs) that were captured during the growth of andalusite in response to regional Permian deformation in the Chinese Altai Orogen.
2) The last crushing steps of gentle stepwise crushing yielded consistent ^{40}Ar/^{39}Ar ages of 282–277 Ma for the andalusites. These ages differ from those of ^{40}Ar/^{39}Ar stepwise heating on muscovite flakes (*ca.* 243–241 Ma) as well as the timing of later sericitization (*ca.* 216 Ma) and chloritization (*ca.* 214 Ma). Moreover, gases released from the andalusite crushing and the subsequent heating experiments show distinct geochemical characteristics in terms of K/Ca ratios and K-, Ca- and Cl-derived argon isotopes. These features collectively suggest negligible interferences from K-bearing solid phases to the ^{40}Ar/^{39}Ar ages of FIPs in andalusites.
3) This study provides new evidence for the preservation of excess ^{40}Ar in K-poor metamorphic nesosilicate minerals. Our data suggest that excess ^{40}Ar is primarily stored in fluid inclusions rather than solid phases such as mineral lattices as previously thought. Circulation of hydrothermal fluids in association with the development of regional penetrative foliations and fracture networks during deformation would create a relatively open environment, which could generate the variable and even air-like initial ^{40}Ar/^{36}Ar ratios of the FIPs in the andalusites.
4) Our new fluid inclusion ^{40}Ar/^{39}Ar ages of andalusites are consistent with monazite U–Pb ages of syn-tectonic leucogranite dykes (275–273 Ma) and other published age constraints of the regional Permian tectono-thermal event, which verifies that the andalusite fluid inclusion ^{40}Ar/^{39}Ar ages represent the formation age of the syn-tectonic quartz veins and hence the corresponding deformation and metamorphism in the region. These results suggest that the ^{40}Ar/^{39}Ar stepwise crushing method can be used to date andalusite which permits additional age constraints on deformation and associated metamorphism in low-pressure metapelitic terranes in general.
5) Combining stepwise crushing experiments on K-poor minerals with stepwise heating experiments on crushed powders and associated K-bearing minerals can help to construct a more complete history of regional tectono-thermal events. The different closure temperatures of these K/Ar systems provide age constraints on deformation, metamorphism, cooling, as

well as later alteration. These pieces of information are essential for the reconstruction of the tectonic evolution of a fossil orogenic belt.

Declaration of Competing Interest

The authors declare that they have no known competing financial interests or personal relationships that could have appeared to influence the work reported in this paper.

ACKNOWLEDGEMENTS

This project was supported by the Guangdong Basic and Applied Basic Research Foundation (No. 2019A1515012190), the National Natural Science Foundation of China (No. 42022017, 41630315, and 41688103), the International Partnership Program of Chinese Academy of Sciences (No. 132744KYSB20190039), the Project funded by China Postdoctoral Science Foundation (No. 2019M663133), and the Director's Fund of Guangzhou Institute of Geochemistry, CAS (No. 2019SZJJ-06). NSF grant EAR-1714892 to Y. Cai is also acknowledged. Editorial suggestions from Associate Editor Fred Jourdan, as well as constructive reviews from Jan Wijbrans and two anonymous reviewers greatly improved the paper. Sincere thanks also go to R. F. Weinberg for editing an earlier version of this manuscript. C.M. Xing and X. Fu are thanked for their assistance with the collection of EPMA data. We also appreciate the helpful discussions with A. Broussolle, K. Xu, T. Shu, and Z.Y. Li. This is contribution No. IS-3131 from GIGCAS.

APPENDIX A. SUPPLEMENTARY MATERIAL

Supplementary data to this article can be found online at https://doi.org/10.1016/j.gca.2022.01.025.

REFERENCES

Aleinikoff J. N., Schenck W. S., Plank M. O., Srogi L., Fanning C. M., Kamo S. L. and Bosbyshell H. (2006) Deciphering igneous and metamorphic events in high-grade rocks of the Wilmington Complex, Delaware: Morphology, cathodoluminescence and backscattered electron zoning, and SHRIMP U-Pb geochronology of zircon and monazite. *Geol. Soc. Am. Bull.* **118**, 39–64.

Bai X. J., Liu M., Hu R. G., Fang Y., Liu X., Tang B. and Qiu H. N. (2021) Well-constrained mineralization ages by integrated ^{40}Ar/^{39}Ar and U-Pb dating techniques for the Xitian W-Sn polymetallic deposit, South China. *Econ. Geol.*. doi.10.5382/econgeo.4889, in press.

Bai X. J., Qiu H. N., Liu W. G. and Mei L. F. (2018) Automatic ^{40}Ar/^{39}Ar dating techniques using multicollector ARGUS VI noble gas mass spectrometer with self-made peripheral apparatus. *J. Earth Sci.* **29**, 408–415.

Bai X. J., Wang M., Jiang Y. D. and Qiu H. N. (2013) Direct dating of tin-tungsten mineralization of the Piaotang tungsten deposit, South China, by ^{40}Ar–^{39}Ar progressive crushing. *Geochim. Cosmochim. Acta* **114**, 1–12.

Bakker R. J. and Schilli S. E. (2016) Formation conditions of leucogranite dykes and aplite-pegmatite dykes in the eastern Mt. Capanne plutonic complex (Elba, Italy): Fluid inclusion studies in quartz, tourmaline, andalusite and plagioclase. *Mineral. Petrol.* **110**, 43–63.

Barredo F. B., Pérez A. P., Montero P. G., Ruiz J. T. and Crespo P. P. G. (2009) Tourmaline ^{40}Ar/^{39}Ar chronology of tourmaline-rich rocks from Central Iberia dates the main Variscan deformation phases. *Geologica Acta* **7**, 399–412.

Baxter E. F. (2003) Quantification of the factors controlling the presence of excess ^{40}Ar or ^{4}He. *Earth Planet. Sci. Lett.* **216**, 619–634.

Bodnar R., Lecumberri-Sanchez P., Moncada D. and Steele-MacInnis M. (2014) 135—Fluid inclusions in hydrothermal ore deposits. In *Treatise on Geochemistry*, second ed. Elsevier, Oxford, pp. 119–142.

Bodnar R. J. and Samson I. (2003) Introduction to fluid inclusions. In *Fluid Inclusions: Analysis and Interpretation* (eds. I. Samson, A. Anderson and D. Marshall). Mineralogical Association of Canada, pp. 1–8.

Bons P. D. (2001) The formation of large quartz veins by rapid ascent of fluids in mobile hydrofractures. *Tectonophysics* **336**, 1–17.

Bosse V. and Villa I. M. (2019) Petrochronology and hygrochronology of tectono-metamorphic events. *Gondwana Res.* **71**, 76–90.

Boullier A. M. (1999) Fluid inclusions: Tectonic indicators. *J. Struct. Geol.* **21**, 1229–1235.

Briggs S. M., Yin A., Manning C. E., Chen Z. L. and Wang X. F. (2009) Tectonic development of the southern Chinese Altai Range as determined by structural geology, thermobarometry, ^{40}Ar/^{39}Ar thermochronology, and Th/Pb ion-microprobe monazite geochronology. *Geol. Soc. Am. Bull.* **121**, 1381–1393.

Briggs S. M., Yin A., Manning C. E., Chen Z. L., Wang X. F. and Grove M. (2007) Late Paleozoic tectonic history of the Ertix Fault in the Chinese Altai and its implications for the development of the Central Asian Orogenic System. *Geol. Soc. Am. Bull.* **119**, 944–960.

Broussolle A., Aguilar C., Sun M., Schulmann K., Štípská P., Jiang Y. D., Yu Y., Xiao W. J., Wang S. and Míková J. (2018) Polycyclic Palaeozoic evolution of accretionary orogenic wedge in the southern Chinese Altai: Evidence from structural relationships and U-Pb geochronology. *Lithos* **314**, 400–424.

Broussolle A., Sun M., Schulmann K., Guy A., Aguilar C., Štípská P., Jiang Y. D., Yu Y. and Xiao W. J. (2019) Are the Chinese Altai "terranes" the result of juxtaposition of different crustal levels during Late Devonian and Permian orogenesis? *Gondwana Res.* **66**, 183–206.

Brown P. E. and Lamb W. M. (1989) P-V-T properties of fluids in the system $H_2O \pm CO_2 \pm NaCl$: New graphical presentations and implications for fluid inclusion studies. *Geochim. Cosmochim. Acta* **53**, 1209–1221.

Bucholz C. E. and Ague J. (2010) Fluid flow and Al transport during quartz-kyanite vein formation, Unst, Shetland Islands, Scotland. *J. Metamorph. Geol.* **28**, 19–39.

Cai K. D., Sun M., Yuan C., Zhao G. C., Xiao W. J., Long X. P. and Wu F. Y. (2011) Prolonged magmatism, juvenile nature and tectonic evolution of the Chinese Altai, NW China: Evidence from zircon U-Pb and Hf isotopic study of Paleozoic granitoids. *J. Asian Earth Sci.* **42**, 949–968.

Cesare B. (1994) Synmetamorphic veining: Origin of andalusite-bearing veins in the Vedrette di Ries contact aureole, Eastern Alps, Italy. *J. Metamorph. Geol.* **12**, 643–653.

Chapman C. A. (1950) Quartz veins formed by metamorphic differentiation of aluminous schists. *Am. Mineral.* **35**, 693–710.

Chen M., Sun M., Li P., Zheng J., Cai K. and Su Y. (2019) Late Paleozoic accretionary and collisional processes along the southern peri-Siberian orogenic system: New constraints from amphibolites within the Irtysh complex of Chinese Altai. *J. Geol.* **127**, 241–262.

Connolly J. (1997) Devolatilization-generated fluid pressure and deformation-propagated fluid flow during prograde regional metamorphism. *J. Geophys. Res.: Solid Earth* **102**, 18149–18173.

Crawford M. and Hollister L. (1986) Metamorphic fluids: the evidence from fluid inclusions. In *Fluid—Rock Interactions during Metamorphism*. Springer, pp. 1–35.

Cui X., Sun M., Zhao G., Yao J., Zhang Y., Han Y. and Dai L. (2020) A Devonian arc–back-arc basin system in the southern Chinese Altai: Constraints from geochemical and Sr-Nd-Pb isotopic data for meta-basaltic rocks. *Lithos* **366** 105540.

Daele J. V., Dewaele S., Melcher F., Onuk P., Spikings R., Glorie S., Jepson G. and Muchez P. (2020) Geochronology of metamorphism, deformation and fluid circulation: A comparison between Rb-Sr and Ar-Ar phyllosilicate and U-Pb apatite systematics in the Karagwe-Ankole Belt (Central Africa). *Gondwana Res.* **83**, 279–297.

Di Vincenzo G., Carosi R. and Palmeri R. (2004) The relationship between tectono-metamorphic evolution and argon isotope records in white mica: Constraints from in situ ^{40}Ar–^{39}Ar laser analysis of the Variscan basement of Sardinia. *J. Petrol.* **45**, 1013–1043.

Di Vincenzo G., Ghiribelli B., Giorgetti G. and Palmeri R. (2001) Evidence of a close link between petrology and isotope records: Constraints from SEM, EMP, TEM and in situ ^{40}Ar–^{39}Ar laser analyses on multiple generations of white micas (Lanterman Range, Antarctica). *Earth Planet. Sci. Lett.* **192**, 389–405.

Dusséaux C., Gébelin A., Boulvais P., Gardien V., Grimes S. and Mulch A. (2019) Meteoric fluid-rock interaction in Variscan shear zones. *Terra Nova* **31**, 366–372.

Fitz-Diaz E., Cottle J. M., Isabel Vidal-Reyes M. and Ben V. D. P. (2019) In situ Th/Pb dating of monazite in fibrous veins: Direct dating of veins and deformation in the shallow upper crust of the Mexican Orogen. *J. Struct. Geol.* **124**, 136–142.

Goldstein R. H. and Reynolds T. J. (1994) Systematics of fluid inclusions in diagenetic minerals. *SEPM Short Course (Society for Sedimentary Geology)* **31**, 199.

Goldstein R. H., Samson I. and Anderson A. (2003) Petrographic analysis of fluid inclusions. *Fluid Inclus.: Anal. Interp.* **32**, 9–53.

Grove M. and Harrison T. M. (1996) ^{40}Ar* diffusion in Fe-rich biotite. *Am. Mineral.* **81**, 940–951.

Harrison T. M., Célérier J., Aikman A. B., Hermann J. and Heizler M. T. (2009) Diffusion of ^{40}Ar in muscovite. *Geochim. Cosmochim. Acta* **73**, 1039–1051.

Harrison T. M., Duncan I. and McDougall I. (1985) Diffusion of ^{40}Ar in biotite: Temperature, pressure and compositional effects. *Geochim. Cosmochim. Acta* **49**, 2461–2468.

Harrison T. M., Heizler M. T. and Lovera O. M. (1993) In vacuo crushing experiments and K-feldspar thermochronometry. *Earth Planet. Sci. Lett.* **117**, 169–180.

Hénocque O., Ruffet G., Colin F. and Féraud G. (1998) ^{40}Ar/^{39}Ar dating of West African lateritic cryptomelanes. *Geochim. Cosmochim. Acta* **62**, 2739–2756.

Hu G. H., Xiao W. J., Wei C. J., Zhao Y. and Liu J. N. (2021) Crustal melting in a protracted hot setting in the Altai Orogen (NW China): Evidence from Permian leucogranite dykes in the metamorphic belt. *Lithos* **384** 105962.

Hu R. G., Bai X. J., Wijbrans J., Brouwer F., Zhao Y. L. and Qiu H. N. (2018) Occurrence of excess ^{40}Ar in amphibole: Implications of ^{40}Ar/^{39}Ar dating by laser stepwise heating and in vacuo crushing. *J. Earth Sci.* **29**, 416–426.

Hu R. G., Wijbrans J., Brouwer F., Zhao L. H., Wang M. and Qiu H. N. (2015) Retrograde metamorphism of the eclogite in North Qaidam, western China: Constraints by joint ^{40}Ar/^{39}Ar in vacuo crushing and stepped heating. *Geosci. Front.* **6**, 759–770.

Huang Y. Q., Jiang Y. D., Collett S., Wang S., Xu K., Shu T., Li P. F. and Yuan C. (2020) Magmatic recycling of accretionary wedge: A new perspective on Silurian-Devonian I-type granitoids generation in the Chinese Altai. *Gondwana Res.* **78**, 291–307.

Jiang Q., Jourdan F., Olierook H. K. H., Merle R. E., Verati C. and Mayers C. (2021a) ^{40}Ar/^{39}Ar dating of basaltic rocks and the pitfalls of plagioclase alteration. *Geochim. Cosmochim. Acta* **314**, 334–357.

Jiang Y. D., Qiu H. N. and Xu Y. G. (2012) Hydrothermal fluids, argon isotopes and mineralization ages of the Fankou Pb-Zn deposit in south China: Insights from sphalerite ^{40}Ar/^{39}Ar progressive crushing. *Geochim. Cosmochim. Acta* **84**, 369–379.

Jiang Y. D., Schulmann K., Kröner A., Sun M., Lexa O., Janoušek V., Buriánek D., Yuan C. and Hanžl P. (2017) Neoproterozoic-early Paleozoic peri-Pacific accretionary evolution of the Mongolian collage system: Insights from geochemical and U-Pb zircon data from the Ordovician sedimentary wedge in the Mongolian Altai. *Tectonics* **36**, 2305–2331.

Jiang Y. D., Schulmann K., Sun M., Štípská P., Guy A., Janoušek V., Lexa O. and Yuan C. (2016) Anatexis of accretionary wedge, Pacific-type magmatism, and formation of vertically stratified continental crust in the Altai Orogenic Belt. *Tectonics* **35**, 3095–3118.

Jiang Y. D., Schulmann K., Sun M., Weinberg R. F., Štípská P., Li P. F., Zhang J., Chopin F., Wang S., Xia X. P. and Xiao W. J. (2019) Structural and geochronological constraints on Devonian suprasubduction tectonic switching and Permian collisional dynamics in the Chinese Altai, central Asia. *Tectonics* **38**, 253–280.

Jiang Y. D., Štípská P., Sun M., Schulmann K., Zhang J., Wu Q. H., Long X. P., Yuan C., Racek M. and Zhao G. C. (2015) Juxtaposition of Barrovian and migmatite domains in the Chinese Altai: A result of crustal thickening followed by doming of partially molten lower crust. *J. Metamorph. Geol.* **33**, 45–70.

Jiang Y. D., Štípská P., Schulmann K., Aguilar C., Wang S., Anczkiewicz R., Zhang J., Li P. F. and Francis C. (2021b) Barrovian and Buchan metamorphic series in the Chinese Altai: P–T–t–D evolution and tectonic implications. *J. Metamorph. Geol.*. doi.10.1111/jmg.12647, in press.

Jourdan F., Féraud G., Bertrand H. and Watkeys M. K. (2007) From flood basalts to the inception of oceanization: Example from the ^{40}Ar/^{39}Ar high-resolution picture of the Karoo large igneous province. *Geochem. Geophys. Geosyst.* **8**, Q02002.

Kelley S. (2002) Excess argon in K-Ar and Ar–Ar geochronology. *Chem. Geol.* **188**, 1–22.

Kelley S., Turner G., Butterfield A. W. and Shepherd T. J. (1986) The source and significance of argon isotopes in fluid inclusions from areas of mineralization. *Earth Planet. Sci. Lett.* **79**, 303–318.

Kendrick M. A. (2007) Comment on 'Paleozoic ages and excess ^{40}Ar in garnets from the Bixiling eclogite in Dabieshan, China: New insights from ^{40}Ar/^{39}Ar dating by stepwise crushing by Hua-Ning Qiu and J.R. Wijbrans'. *Geochim. Cosmochim. Acta* **71**, 6040–6045.

Kendrick M. A. and Burnard P. (2013) Noble gases and halogens in fluid inclusions: a journey through the Earth's crust. In *The Noble Gases as Geochemical Tracers* (ed. P. Burnard). Springer-Verlag, Berlin, pp. 319–369.

Kendrick M. A. and Phillips D. (2009) New constraints on the release of noble gases during in vacuo crushing and application to scapolite Br–Cl–I and ^{40}Ar/^{39}Ar age determinations. *Geochim. Cosmochim. Acta* **73**, 5673–5692.

Kennedy B. M. and Van Soest M. C. (2007) Flow of mantle fluids through the ductile lower crust: Helium isotope trends. *Science* **318**, 1433–1436.

Kröner A., Windley B., Badarch G., Tomurtogoo O., Hegner E., Jahn B., Gruschka S., Khain E., Demoux A. and Wingate M. (2007) Accretionary growth and crust formation in the Central Asian Orogenic Belt and comparison with the Arabian-Nubian shield. *Geol. Soc. Am. Mem.* **200**, 181.

Lacombe O. and Rolland Y. (2016) Fluids in crustal deformation: Fluid flow, fluid-rock interactions, rheology, melting and resources. *J. Geodyn.* **101**, 1–4.

Laurent-Charvet S., Charvet J., Monié P. and Shu L. (2003) Late Paleozoic strike-slip shear zones in eastern Central Asia (NW China): New structural and geochronological data. *Tectonics* **22**, 1009.

Lee J. Y., Marti K., Severinghaus J. P., Kawamura K., Yoo H. S., Lee J. B. and Kim J. S. (2006) A redetermination of the isotopic abundances of atmospheric Ar. *Geochim. Cosmochim. Acta* **70**, 4507–4512.

Lehmann J., Schulmann K., Lexa O., Corsini M., Kröner A., Štípská P., Tomurhuu D. and Otgonbator D. (2010) Structural constraints on the evolution of the Central Asian Orogenic Belt in SW Mongolia. *Am. J. Sci.* **310**, 575–628.

Lespinasse M. (1999) Are fluid inclusion planes useful in structural geology? *J. Struct. Geol.* **21**, 1237–1243.

Li P. F., Sun M., Rosenbaum G., Cai K. D. and Yu Y. (2015) Structural evolution of the Irtysh Shear Zone (northwestern China) and implications for the amalgamation of arc systems in the Central Asian Orogenic Belt. *J. Struct. Geol.* **80**, 142–156.

Li P. F., Sun M., Rosenbaum G., Jiang Y. D. and Cai K. D. (2016) Structural evolution of zonal metamorphic sequences in the southern Chinese Altai and relationships to Permian transpressional tectonics in the Central Asian Orogenic Belt. *Tectonophysics* **693**, 277–289.

Li P. F., Sun M., Rosenbaum G., Jourdan F., Li S. Z. and Cai K. D. (2017) Late Paleozoic closure of the Ob-Zaisan Ocean along the Irtysh shear zone (NW China): Implications for arc amalgamation and oroclinal bending in the Central Asian orogenic belt. *Geol. Soc. Am. Bull.* **129**, 547–569.

Li Z. L., Yang X. Q., Li Y. Q., Santosh M., Chen H. L. and Xiao W. J. (2014) Late Paleozoic tectono–metamorphic evolution of the Altai segment of the Central Asian Orogenic Belt: Constraints from metamorphic P-T pseudosection and zircon U–Pb dating of ultra-high-temperature granulite. *Lithos* **204**, 83–96.

Lin Z. F., Yuan C., Zhang Y. Y., Sun M., Long X. P., Wang X. Y., Huang Z. Y. and Chen Z. W. (2019) Petrogenesis and geodynamic implications of two episodes of Permian and Triassic high-silica granitoids in the Chinese Altai, Central Asian Orogenic Belt. *J. Asian Earth Sci.* **184** 103978.

Liu F. and Han D. (2019) Petrogenetic and tectonic implications of Triassic granitoids in the Chinese Altay: The Alaer granite example. *Heliyon* **5** e01261.

Liu F., Zhang Z. X., Li Q., Zhang C. and Li C. (2014) New precise timing constraint for the Keketuohai No. 3 pegmatite in Xinjiang, China, and identification of its parental pluton. *Ore Geol. Rev.* **56**, 209–219.

Liu Y. S., Hu Z. C., Gao S., Günther D., Xu J., Gao C. G. and Chen H. H. (2008) In situ analysis of major and trace elements of anhydrous minerals by LA-ICP-MS without applying an internal standard. *Chem. Geol.* **257**, 34–43.

Liu Z., Bartoli O., Tong L. X., Carvalho B. B. and Li C. (2020) Anatexis and metamorphic history of Permian pelitic granulites from the southern Chinese Altai: Constraints from petrology, melt inclusions and phase equilibria modelling. *Lithos* **360–361** 105432.

Liu Z., Bartoli O., Tong L. X., Xu Y. G. and Huang X. L. (2019) Permian ultrahigh–temperature reworking in the southern Chinese Altai: Evidence from petrology, P-T estimates, zircon and monazite U–Th–Pb geochronology. *Gondwana Res.* **78**, 20–40.

Long X. P., Sun M., Yuan C., Xiao W. J. and Cai K. (2008) Early Paleozoic sedimentary record of the Chinese Altai: Implications for its tectonic evolution. *Sediment. Geol.* **208**, 88–100.

Ludwig K. (2001) *Users manual for Isoplot/Ex (rev. 2.49): A geochronological toolkit for Microsoft Excel (Special Publication No. 1a, 55 p)*. Berkeley Geochronology Center.

Lv Z. H., Zhang H. and Tang Y. (2021) Anatexis origin of rare metal/earth pegmatites: Evidences from the Permian pegmatites in the Chinese Altai. *Lithos* **380** 105865.

Lv Z. H., Zhang H., Tang Y., Liu Y. L. and Zhang X. (2018) Petrogenesis of syn-orogenic rare metal pegmatites in the Chinese Altai: Evidences from geology, mineralogy, zircon U-Pb age and Hf isotope. *Ore Geol. Rev.* **95**, 161–181.

Mancktelow N., Zwingmann H., Campani M., Fügenschuh B. and Mulch A. (2015) Timing and conditions of brittle faulting on the Silltal-Brenner fault zone, Eastern Alps (Austria). *Swiss J. Geosci.* **108**, 305–326.

Masoudi F., Mehrabi B., Aghdam M. R. and Yardley B. W. D. (2009) The nature of fluids during pegmatite development in metamorphic terrains: Evidence from Hamadan complex, Sanandaj-Sirjan metamorphic zone, Iran. *J. Geol. Soc. India* **73**, 407–418.

Matsumoto T., Chen Y. and Matsuda J. I. (2001) Concomitant occurrence of primordial and recycled noble gases in the Earth's mantle. *Earth Planet. Sci. Lett.* **185**, 35–47.

Menzies C. D., Teagle D. A. H., Craw D., Cox S. C., Boyce A. J., Barrie C. D. and Roberts S. (2014) Incursion of meteoric waters into the ductile regime in an active orogen. *Earth Planet. Sci. Lett.* **399**, 1–13.

Nabelek and Peter I. (1997) Quartz-sillimanite leucosomes in high-grade schists, Black Hills, South Dakota: A perspective on the mobility of Al in high-grade metamorphic rocks. *Geology* **25**, 995–998.

Oliver N. H. S. (1996) Review and classification of structural controls on fluid flow during regional metamorphism. *J. Metamorph. Geol.* **14**, 477–492.

Qiu H. N. and Dai T. M. (1989) ^{40}Ar/^{39}Ar technique for dating the fluid Inclusions of quartz from a hydrothermal deposit. *Chin. Sci. Bull.* **34**, 1887–1890.

Qiu H. N. and Jiang Y. D. (2007) Sphalerite ^{40}Ar/^{39}Ar progressive crushing and stepwise heating techniques. *Earth Planet. Sci. Lett.* **256**, 224–232.

Qiu H. N., Pu Z. P. and Dai T. M. (2007) Occurrences of Excess ^{40}Ar in hydrothermal tourmaline: Interpretations from ^{40}Ar-^{39}-Ar dating results by stepwise heating. *Acta Geol. Sin.-English Edition* **81**, 510–516.

Qiu H. N. and Wijbrans J. R. (2006) Paleozoic ages and excess ^{40}Ar in garnets from the Bixiling eclogite in Dabieshan, China: New insights from ^{40}Ar/^{39}Ar dating by stepwise crushing. *Geochim. Cosmochim. Acta* **70**, 2354–2370.

Qiu H. N., Wijbrans J. R., Brouwer F. M., Yun J. B., Zhao L. H. and Xu Y. G. (2010) Amphibolite facies retrograde metamorphism of the Zhujiachong eclogite, SE Dabieshan: ^{40}Ar/^{39}Ar age constraints from argon extraction using UV-laser microprobe, in vacuo crushing and stepwise heating. *J. Metamorph. Geol.* **28**, 477–487.

Qiu H. N., Wu H. Y., Yun J. B., Feng Z. H., Xu Y. G., Mei L. F. and Wijbrans J. R. (2011) High-precision ^{40}Ar–^{39}Ar age of the gas emplacement into the Songliao Basin. *Geology* **39**, 451–454.

Qu G. S. and Zhang J. J. (1994) Oblique thrust systems in the Altay orogeny, China. *J. Southeast Asian Earth Sci.* **9**, 277–287.

Rauchenstein-Martinek K., Wagner T., Wälle M., Heinrich C. A. and Arlt T. (2016) Chemical evolution of metamorphic fluids in the Central Alps, Switzerland: Insight from LA-ICPMS analysis of fluid inclusions. *Geofluids* **16**, 877–908.

Ren Z. and Vasconcelos P. M. (2019) Quantifying ^{39}Ar recoil in natural hypogene and supergene alunites and jarosites. *Geochim. Cosmochim. Acta* **260**, 84–98.

Roedder E. (1984) *Fluid inclusions, Reviews in Mineralogy*. Mineralogical Society of America, Washington, p. 644.

Scarsi P. (2000) Fractional extraction of helium by crushing of olivine and clinopyroxene phenocrysts: Effects on the ^{3}He/^{4}He measured ratio. *Geochim. Cosmochim. Acta* **64**, 3751–3762.

Schaen A. J., Jicha B. R., Hodges K. V., Vermeesch P., Stelten M. E., Mercer C. M., Phillips D., Rivera T. A., Jourdan F., Matchan E. L., Hemming S. R., Morgan L. E., Kelley S. P., Cassata W. S., Heizler M. T., Vasconcelos P. M., Benowitz J. A., Koppers A. A. P., Mark D. F., Niespolo E. M., Sprain C. J., Hames W. E., Kuiper K. F., Turrin B. D., Renne P. R., Ross J., Nomade S., Guillou H., Webb L. E., Cohen B. A., Calvert A. T., Joyce N., Ganerød M., Wijbrans J., Ishizuka O., He H., Ramirez A., Pfänder J. A., Lopez-Martínez M., Qiu H. and Singer B. S. (2021) Interpreting and reporting ^{40}Ar/^{39}Ar geochronologic data. *Geol. Soc. Am. Bull.* **3–4**, 461–487.

Şengör A. M. C. and Natal'In B. A. (1996) Paleotectonics of Asia: fragments of a synthesis. In *The tectonic evolution of Asia* (eds. A. Yin and T. M. Harrison). Cambridge University Press, New York, pp. 486–640.

Şengör A. M. C., Natal'In B. A. and Burtman V. S. (1993) Evolution of the Altaid tectonic collage and Palaeozoic crustal growth in Eurasia. *Nature* **364**, 299.

Sepahi A. A., Whitney D. L. and Baharifar A. A. (2004) Petrogenesis of andalusite-kyanite-sillimanite veins and host rocks, Sanandaj-Sirjan metamorphic belt, Hamadan, Iran. *J. Metamorph. Geol.* **22**, 119–134.

Shepherd T. J. and Darbyshire D. P. F. (1981) Fluid inclusion Rb–Sr isochrons for dating mineral deposits. *Nature* **290**, 578–579.

Siebenaller L., Vanderhaeghe O., Jessell M., Boiron M.-C. and Hibsch C. (2016) Syntectonic fluids redistribution and circulation coupled to quartz recrystallization in the ductile crust (Naxos Island, Cyclades, Greece). *J. Geodyn.* **101**, 129–141.

Steiger R. H. and Jäger E. (1977) Subcommission on geochronology: Convention on the use of decay constants in geo-and cosmochronology. *Earth Planet. Sci. Lett.* **36**, 359–362.

Thern E. R., Blereau E., Jourdan F. and Nelson D. R. (2020) Tourmaline ^{40}Ar/^{39}Ar geochronology and thermochronology: Example from Hadean-zircon-bearing siliciclastic metasedimentary rocks from the Yilgarn Craton. *Geochim. Cosmochim. Acta* **277**, 285–299.

Tong L. X., Xu Y. G., Cawood P. A., Zhou X., Chen Y. B. and Liu Z. (2014) Anticlockwise P-T evolution at similar to 280 Ma recorded from ultrahigh-temperature metapelitic granulite in the Chinese Altai orogenic belt, a possible link With the Tarim mantle plume? *J. Asian Earth Sci.* **94**, 1–11.

Turner G. and Wang S. S. (1992) Excess argon, crustal fluids and apparent isochrons from crushing K-feldspar. *Earth Planet. Sci. Lett.* **110**, 193–211.

Verati C. and Jourdan F. (2014) Modelling effect of sericitization of plagioclase on the ^{40}K/^{40}Ar and ^{40}Ar/^{39}Ar chronometers: Implication for dating basaltic rocks and mineral deposits. *Geological Society, London, Special Publications* **378**, 155–174.

Villa I. M. (2001) Radiogenic isotopes in fluid inclusions. *Lithos* **55**, 115–124.

Villa I. M. (2016) Diffusion in mineral geochronometers: Present and absent. *Chem. Geol.* **420**, 1–10.

Villa I. M., Bucher S., Bousquet R., Kleinhanns I. C. and Schmid S. M. (2014) Dating polygenetic metamorphic assemblages along a transect across the Western Alps. *J. Petrol.* **55**, 803–830.

Villa I. M., Grobéty B., Kelley S. P., Trigila R. and Wieler R. (1996) Assessing Ar transport paths and mechanisms in the McClure Mountains hornblende. *Contrib. Mineral. Petrol.* **126**, 67–80.

Villa I. M. and Hanchar J. M. (2017) Age discordance and mineralogy. *Am. Mineral.* **102**, 2422–2439.

Wang S. J., Wang L., Brown M., Piccoli P. M., Johnson T. E., Feng P., Deng H., Kitajima K. and Huang Y. (2017) Fluid generation and evolution during exhumation of deeply subducted UHP continental crust: Petrogenesis of composite granite–quartz veins in the Sulu belt, China. *J. Metamorph. Geol.* **35**, 601–629.

Wang S. S. (1983) Age determinations of ^{40}Ar–^{40}K, ^{40}Ar–^{39}Ar and radiogenic ^{40}Ar released characteristics on K-Ar geostandards of China. *Chin. J. Geol.*, 315–323, in Chinese with English abstract.

Wang T., Hong D. W., Jahn B. M., Tong Y., Wang Y. B., Han B. F. and Wang X. X. (2006) Timing, petrogenesis, and setting of Paleozoic synorogenic intrusions from the Altai Mountains, Northwest China: Implications for the tectonic evolution of an accretionary orogen. *J. Geol.* **114**, 735–751.

Wang T., Jahn B.-M., Kovach V. P., Tong Y., Wilde S. A., Hong D. W., Li S. and Salnikova E. B. (2014a) Mesozoic intraplate granitic magmatism in the Altai accretionary orogen, NW China: Implications for the orogenic architecture and crustal growth. *Am. J. Sci.* **314**, 1–42.

Wang T., Tong Y., Jahn B.-M., Zou T. R., Wang Y. B., Hong D. W. and Han B. F. (2007) SHRIMP U-Pb zircon geochronology of the Altai No. 3 pegmatite, NW China, and its implications for the origin and tectonic setting of the pegmatite. *Ore Geol. Rev.* **32**, 325–336.

Wang W., Wei C. J., Wang T., Lou Y. X. and Chu H. (2009) Confirmation of pelitic granulite in the Altai orogen and its geological significance. *Chin. Sci. Bull.* **54**, 2543–2548.

Wang W., Wei C. J., Zhang Y. H., Chu H., Zhao Y. and Liu X. C. (2014b) Age and origin of sillimanite schist from the Chinese Altai metamorphic belt: Implications for late Palaeozoic tectonic evolution of the Central Asian Orogenic Belt. *Int. Geol. Rev.* **56**, 224–236.

Wei C. J., Clarke G., Tian W. and Qiu L. (2007) Transition of metamorphic series from the Kyanite- to andalusite-types in the Altai orogen, Xinjiang, China: Evidence from petrography and calculated KMnFMASH and KFMASH phase relations. *Lithos* **96**, 353–374.

Whitney D. L. and Dilek Y. (2000) Andalusite-sillimanite-quartz veins as indicators of low-pressure-high-temperature deformation during late-stage unroofing of a metamorphic core complex, Turkey. *J. Metamorph. Geol.* **18**, 59–66.

Windley B. F., Alexeiev D., Xiao W., Kröner A. and Badarch G. (2007) Tectonic models for accretion of the Central Asian Orogenic Belt. *J. Geol. Soc.* **164**, 31–47.

Windley B. F., Kröner A., Guo J., Qu G., Li Y. and Zhang C. (2002) Neoproterozoic to Paleozoic geology of the Altai orogen, NW China: New zircon age data and tectonic evolution. *J. Geol.* **110**, 719–737.

Xiao M., Jiang Y. D., Qiu H. N., Cai Y. and Zhang W. F. (2022) An improved gas extraction model during stepwise crushing: New perspectives on fluid geochronology and geochemistry. *Ore Geol. Rev.* **140** 104588.

Xiao M., Qiu H. N., Cai Y., Jiang Y. D., Zhang W. F. and Fang Y. (2021) Progressively released gases from fluid inclusions reveal new insights on W-Sn mineralization of the Yaogangxian tungsten deposit, South China. *Ore Geol. Rev.* **138** 104353.

Xiao M., Qiu H. N., Jiang Y. D., Cai Y., Bai X. J., Zhang W. F., Liu M. and Qin C. J. (2019) Gas release systematics of mineral-hosted fluid inclusions during stepwise crushing: Implications for ^{40}Ar/^{39}Ar geochronology of hydrothermal fluids. *Geochim. Cosmochim. Acta* **251**, 36–55.

Xiao W. J., Windley B. F., Badarch G., Sun S., Li J., Qin K. Z. and Wang Z. H. (2004) Palaeozoic accretionary and convergent tectonics of the southern Altaids: Implications for the growth of Central Asia. *J. Geol. Soc.* **161**, 339–342.

Xiao W. J., Windley B. F., Sun S., Li J. L., Huang B. C., Han C. M., Yuan C., Sun M. and Chen H. L. (2015) A Tale of Amalgamation of Three Permo-Triassic Collage Systems in Central Asia: Oroclines, Sutures, and Terminal Accretion. *Annu. Rev. Earth Planet. Sci.* **43**, 477–507.

Xiao W. J., Windley B. F., Yuan C., Sun M., Han C. M., Lin S. F., Chen H. L., Yan Q. R., Liu D. Y., Qin K. Z., Li J. L. and Sun S. (2009) Paleozoic multiple subduction-accretion processes of the southern Altaids. *Am. J. Sci.* **309**, 221–270.

Xu K., Jiang Y. D., Wang S., Shu T., Li Z. Y., Collett S., Yuan C. and Kong L. Z. (2021) Multi-phase tectonothermal evolution in the SE Chinese Altai, central Asia: Structures, U-Pb monazite ages and tectonic implications. *Lithos* **392** 106148.

Yardley B. W. D. and Bottrell S. H. (1992) Silica mobility and fluid movement during metamorphism of the Connemara schists, Ireland. *J. Metamorph. Geol.* **10**, 453–464.

Yuan C., Sun M., Xiao W., Li X., Chen H., Lin S., Xia X. P. and Long X. (2007) Accretionary orogenesis of the Chinese Altai: Insights from Paleozoic granitoids. *Chem. Geol.* **242**, 22–39.

Yun J. B., Wu H. Y., Feng Z. H., Mei L. F. and Qiu H. N. (2010) CO_2 gas emplacement age in the Songliao Basin: Insight from volcanic quartz ^{40}Ar–^{39}Ar stepwise crushing. *Chin. Sci. Bull.* **55**, 1795–1799.

Zhang C. L., Santosh M., Zou H. B., Xu Y. G., Zhou G., Dong Y. G., Ding R. F. and Wang H. Y. (2012) Revisiting the "Irtish tectonic belt": Implications for the Paleozoic tectonic evolution of the Altai orogen. *J. Asian Earth Sci.* **52**, 117–133.

Zhang J., Sun M., Schulmann K., Zhao G. C., Wu Q. H., Jiang Y. D., Guy A. and Wang Y. J. (2015) Distinct deformational history of two contrasting tectonic domains in the Chinese Altai: Their significance in understanding accretionary orogenic process. *J. Struct. Geol.* **73**, 64–82.

Zhang W. F., Zheng D. W., Liu G. Q., Xu Y. G. and Jiang Y. (2021) Optimization of irradiation parameters for ^{40}Ar/^{39}Ar dating by Argus VI multi-collector mass spectrometry. *J. Anal. At. Spectrom.* **36**, 1374–1380.

Zheng C. Q., Kato T., Enami M. and Xu X. C. (2007a) CHIME monazite ages of metasediments from the Altai orogen in northwestern China: Devonian and Permian ages of metamorphism and their significance. *Isl. Arc* **16**, 598–604.

Zheng Y. F., Gao T. S., Wu Y. B., Gong B. and Liu X. M. (2007b) Fluid flow during exhumation of deeply subducted continental crust: Zircon U-Pb age and O-isotope studies of a quartz vein within ultrahigh-pressure eclogite. *J. Metamorph. Geol.* **25**, 267–283.

Zong K. Q., Klemd R., Yuan Y., He Z. Y., Guo J. L., Shi X. L., Liu Y. S., Hu Z. C. and Zhang Z. M. (2017) The assembly of Rodinia: The correlation of early Neoproterozoic (ca. 900 Ma) high-grade metamorphism and continental arc formation in the southern Beishan Orogen, southern Central Asian Orogenic Belt (CAOB). *Precambrian Res.* **290**, 32–48.

Associate editor: Fred Jourdan